

# Formation of H<sub>2</sub>-He substellar bodies in cold conditions: Gravitational stability of binary mixtures in a phase transition

A. Füglistaler and D. Pfenniger

Geneva Observatory, University of Geneva, Sauverny, Switzerland  
e-mail: andreas.fueglistaler@unige.ch

Received 16 July 2015/ Accepted 25 March 2016

## ABSTRACT

**Context.** Molecular clouds typically consist of 3/4 H<sub>2</sub>, 1/4 He and traces of heavier elements. In an earlier work we showed that at very low temperatures and high densities, H<sub>2</sub> can be in a phase transition leading to the formation of ice clumps as large as comets or even planets. However, He has very different chemical properties and no phase transition is expected before H<sub>2</sub> in dense interstellar medium (ISM) conditions. The gravitational stability of fluid mixtures has been studied before, but these studies did not include a phase transition.

**Aims.** We study the gravitational stability of binary fluid mixtures with special emphasis on when one component is in a phase transition. The numerical results are aimed at applications in molecular cloud conditions, but the theoretical results are more general. **Methods.** First, we study the gravitational stability of van der Waals fluid mixtures using linearized analysis and examine virial equilibrium conditions using the Lennard-Jones intermolecular potential. Then, combining the Lennard-Jones and gravitational potentials, the non-linear dynamics of fluid mixtures are studied via computer simulations using the molecular dynamics code LAMMPS.

**Results.** Along with the classical, ideal-gas Jeans instability criterion, a fluid mixture is always gravitationally unstable if it is in a phase transition because compression does not increase pressure. However, the condensed phase fraction increases. In unstable situations the species can separate: in some conditions He precipitates faster than H<sub>2</sub>, while in other conditions the converse occurs. Also, for an initial gas phase collapse the geometry is essential. Contrary to spherical or filamentary collapses, sheet-like collapses starting below 15 K easily reach H<sub>2</sub> condensation conditions because then they are fastest and both the increase of heating and opacity are limited.

**Conclusions.** Depending on density, temperature and mass, either rocky H<sub>2</sub> planetoids, or gaseous He planetoids form. H<sub>2</sub> planetoids are favoured by high density, low temperature and low mass, while He planetoids need more mass and can form at temperature well above the critical value.

**Key words.** Instabilities – ISM: clouds – ISM: kinematics and dynamics – ISM: molecules – Methods: analytical – Methods: numerical

## 1. Introduction

Typically, the Milky Way molecular clouds consist of molecular hydrogen (<sup>1</sup>H<sub>2</sub>) and helium (<sup>4</sup>He) in the respective mass fraction of ~74% and ~24% and traces of heavier elements in the form of atoms, molecules, and dust grains (Draine 2011). The He mass fraction is thus non-negligible. Even though H<sub>2</sub> and He are by far the most abundant chemical components, they remain hardly detectable, and most of the time they are inferred from CO emissions (Bolatto et al. 2013). Thus, the dynamical and chemical processes associated with H<sub>2</sub> and He in molecular clouds are still poorly known, especially when considering sub-AU scales.

In Füglistaler & Pfenniger (2015, hereafter FP2015), we discussed substellar fragmentation including gravity in single species fluids presenting a phase transition, such as very cold molecular hydrogen in molecular cloud conditions. We showed that fluids in a phase transition (i.e. subject to a chemical instability) are anyway also gravitationally unstable because any density fluctuation is not compensated by a pressure variation, but by a change in condensed matter fraction. In phase transition conditions arbitrary small condensed clumps can form. The possibility of forming H<sub>2</sub> ice clumps in the ISM, from grains, to comet-like bodies to rocky or gaseous planet-like bodies pro-

vides a scenario for baryonic dark matter extending the scenario of Pfenniger et al. (1994); Pfenniger & Combes (1994) towards micro-AU scales. However, since molecular clouds contain a substantial fraction of He, it is necessary to investigate how this component might modify the findings of our previous study.

Although at first sight from the chemical point of view both H<sub>2</sub> and He present an outer electronic shell made of two electrons, their chemical properties differ markedly, mainly because of quantum physics. The individual properties of H<sub>2</sub> and He are well known from laboratory data (Air Liquide 1976) and shown in Fig. 1. H<sub>2</sub> and He are in a phase transition when on the condensation wall linking the gaseous and solid or liquid phase. He has a lower critical temperature than H<sub>2</sub> (5.2 K vs. 32.9 K) and a lower critical pressure (0.227 MPa vs. 1.286 MPa). In the highly dynamical conditions present in molecular clouds, such as supersonic turbulence (Elmegreen & Scalo 2004), phase transition conditions may be reached thanks to a combination of pressure increase and/or temperature decrease. In such a case, phase transition conditions are reached for H<sub>2</sub> well before He. The conditions of phase transition of the mixture H<sub>2</sub>-He may, however, change the conclusions made in the single species case.

The properties of H<sub>2</sub>-He mixtures has been mostly studied in detail for temperatures above the critical and at high densi-

ties (e.g. Streett 1973; Koci et al. 2007; Becker et al. 2014) and especially in conditions similar to gas giant planets (Vorberger et al. 2007; Saumon et al. 1995). Taking quantum effects into account, Sasa & Pfenniger (2008) calculate the thermodynamic properties of H<sub>2</sub>-He mixtures below critical temperature from the known intermolecular potentials and obtain the critical point and stability of the mixture itself.

The gravitational stability of self-gravitating binary and multicomponent fluids has been studied by Grishchuk & Zeldovich (1981), who showed that there can be only one unstable solution. If a fluid mixture is gravitationally unstable then all components are affected. They note that in the case  $(\partial P/\partial \rho)_s = 0$  (i.e. the sound-velocity formally vanishes), which is the case in a phase transition, the fluid is always gravitationally unstable, but they do not go into more detail on that specific case. Jog & Solomon (1984a,b) first discussed the stability of two-component disks. In a similar fashion de Carvalho & Macedo (1995) studied oscillations and resonances in a binary fluid mixture. Volkov & Ortega (2000) discussed the stability of self-gravitating systems with a spectrum of particle masses and consider rotating mediums.

When a phase transition occurs in the presence of external or internal gravity, the fluid dense phase may precipitate in the form of rain, snow, or hail in the atmosphere, leading to a fragmentation that is impossible to describe with usual hydrodynamic codes, in which a single phase in local thermal equilibrium is implicitly assumed. In FP2015 we showed that method phase transition and precipitation can be simulated for a single species with molecular dynamics. The possible objects condensing from the gaseous phase can take various masses, typically covering the entire range from grains, comets to planets or larger. With two species with different molecular weights the number of precipitation scenarios that can be envisioned increases. Could it be, for example, that bodies form with a core made of solid H<sub>2</sub> surrounded with an atmosphere of H<sub>2</sub> and He or that a solid H<sub>2</sub> crust floats on a gaseous He core?

To answer such questions we use the same molecular dynamics code as in FP2015 just adding a second species, and scaling the particles properties to the respective properties of H<sub>2</sub> and He. We control the finite number resolution effects by performing simulations over a range from  $1.25 \cdot 10^5$  to  $80 \cdot 10^5$  particles. We restrict the investigations to the simplest set-up combining gravity with molecular dynamics. To control gravitational instability, we investigate a single plane-parallel collapse in one direction of a periodic cube, where the initial temperature and density are simulation parameters. As explained in Sect. 2.2 and Appendix B, the collapse geometry (sheet-, filament-, or point-like) is crucial to reach phase transition conditions starting from typical ISM conditions. Sheet-like collapses (pancakes) can indeed lead temporarily to very dense conditions without much heating, contrary to the other cases.

## 2. Gravitational stability of a fluid mixture

In a fluid consisting of  $K$  different components  $i$ , the total mixture number density is  $n = \sum_i n_i$ , the mixture mass density is  $\rho = \sum_i \rho_i$  with  $\rho_i = m_i n_i$ , and the mixture pressure is  $P = \sum_i P_i$ . In the case of an ideal gas, Dalton's law states  $P = \sum_i x_i P_i$ . Each component has a molecular fraction  $x_i = n_i/n$  and a mass fraction  $w_i = m_i/m$  with  $m = \sum_i x_i m_i$ .

The notion of global temperature in a system with long-range forces is an unsettled topic as the key assumption of extensivity in thermodynamics breaks down in long-range force systems (e.g. Padmanabhan 1990). When dealing with particle systems we can however always define the temperature as proportional

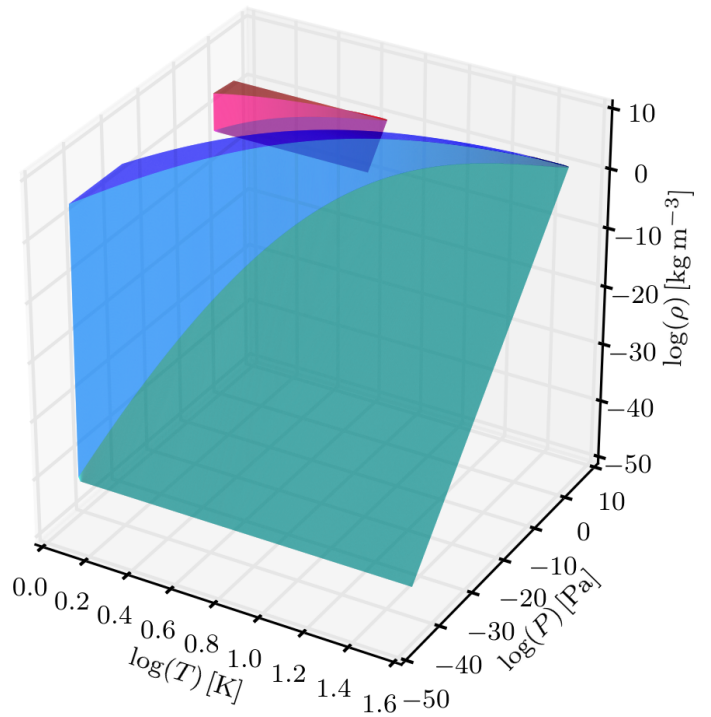


Fig. 1: H<sub>2</sub> (blue) and He (red) phase diagrams. For clarity, only a part of the upper, almost constant density condensed phases of both species and the low-density gas phase of He are shown.

to the residual kinetic energy when the bulk translational, expansional, and rotational velocities are subtracted, be it globally or locally. Strictly, this definition is operational and useful only if the velocity distribution is unimodal and its second order moment exists. Further detailed discussion about this topic would be out of scope, as in this article we consider either global or local temperatures for particle systems with no or negligible amount of ordered motion, so the stated temperature is equivalent to the particle kinetic energy. The high degree of collisionality in molecular interactions ensures the rapid destruction of any initial correlations leading to the convergence towards thermal states.

### 2.1. Jeans instability

Considering a fluid mixture as a one-component fluid using average quantities such as the density  $\rho$  and pressure  $P$ , the Jeans instability criterion (see App. A.1) would be

$$k^2 < k_J^2 \equiv \frac{4\pi G \rho}{(\partial P/\partial \rho)_s}, \quad (1)$$

where  $k$  is the wavenumber,  $k_J$  the critical Jeans wavenumber, and  $G$  the gravitational constant. This is, however, inappropriate if each component has a different mean square velocity, which is the case for an isothermal fluid with different molecular masses.

In order to correctly predict the stability of a many-component fluid mixture with different densities  $\rho_i$  and partial pressure  $P_i$ , each component has to be treated individually: the Grishchuk-Zeldovich criterion (see App. A.2), which is the sum of each component Jeans' criteria, reads

$$k^2 < k_{GZ}^2 \equiv \sum_i \frac{4\pi G \rho_i}{\partial P_i / \partial \rho_i}. \quad (2)$$

### 2.1.1. Ideal gas mixture

A fluid far from the condensed phase can be approximated with the ideal gas law

$$P = nk_B T, \quad (3)$$

$$\left(\frac{\partial P}{\partial \rho}\right)_s = \gamma \frac{k_B T}{m}, \quad (4)$$

where  $k_B$  is the Boltzmann constant,  $\gamma$  the adiabatic index, and  $m$  the molecular mass. The partial pressures can be calculated using Dalton's law. Equ. (2) becomes

$$k_{GZ,id}^2 = \frac{4\pi G}{\gamma k_B T} \sum_i n_i m_i^2, \quad (5)$$

where id stands for ideal gas. This equation differs from Equ. (1), which in the ideal gas case becomes

$$k_{J,id}^2 = \frac{4\pi G}{\gamma k_B T} n m^2. \quad (6)$$

In the case where all components have the same temperature  $k_{GZ,id} \geq k_{J,id}$  independent of the molecular fractions  $x_i = n_i/n$  and molecular mass  $m_i$ . In the case of a H<sub>2</sub>-He mixture, the maximum  $k_{GZ,id}^2/k_{J,id}^2 = 1.12$  at  $x_{H_2} = 0.67$ .

### 2.1.2. van der Waals fluid mixture

When approaching a phase transition, the ideal gas law does not take into account condensations and does not yield correct values anymore. We showed in FP2015 that the van der Waals equation of state (van der Waals 1910) describes a phase transition rather well provided that the Maxwell construct is taken into account (Clerk-Maxwell 1875; Johnston 2014), i.e.

$$P_r = \frac{8T_r}{\frac{3}{n_r} - 1} - 3n_r^2, \quad (7)$$

$$\left(\frac{\partial P_r}{\partial \rho}\right)_s = \gamma \left( \frac{24T_r}{m(n_r - 3)^2} - \frac{6n_r}{m} \right), \quad (8)$$

in gaseous and solid/liquid form with the reduced values  $P_r = P/P_c$ ,  $T_r = T/T_c$ ,  $n_r = n/n_c$  and the critical pressure, temperature and density  $P_c$ ,  $T_c$  and  $n_c$ . In the case of a phase transition,  $P_r = \text{const}$  (Maxwell construct) and  $(\partial P_r / \partial \rho)_s = 0$ .

The Maxwell line is very similar to the laboratory condensation line for H<sub>2</sub> in a  $T - P$  diagram as can be seen in Fig. 2, but is rather off for He, especially at low temperatures. As in the astrophysical context, correctly representing the H<sub>2</sub> phase transition is essential for our study. A H<sub>2</sub> phase transition always occurs at a lower pressure-temperature ratio than for He.

In the phase transition regime  $(\partial P / \partial \rho)_s = 0$ , varying density allows the pressure to remain constant. This is a crucial property for this work, since gravitational contraction is no longer compensated by pressure increase. We show in App. A.2 that a two-component fluid is always gravitationally unstable as soon as  $(\partial P_i / \partial \rho_i)_s = 0$  for any component  $i$ . In a similar fashion, the same can be deduced for  $n$ -component fluids (Grishchuk & Zel'dovich 1981).

### 2.2. Plane-parallel collapse

Lin et al. (1965) and Zel'dovich (1970) show that a plane-parallel collapse, leading to a sheet-like geometry, is a faster collapse than filament- or point-like geometries. This has been confirmed using numerical simulations by Shandarin et al. (1995).

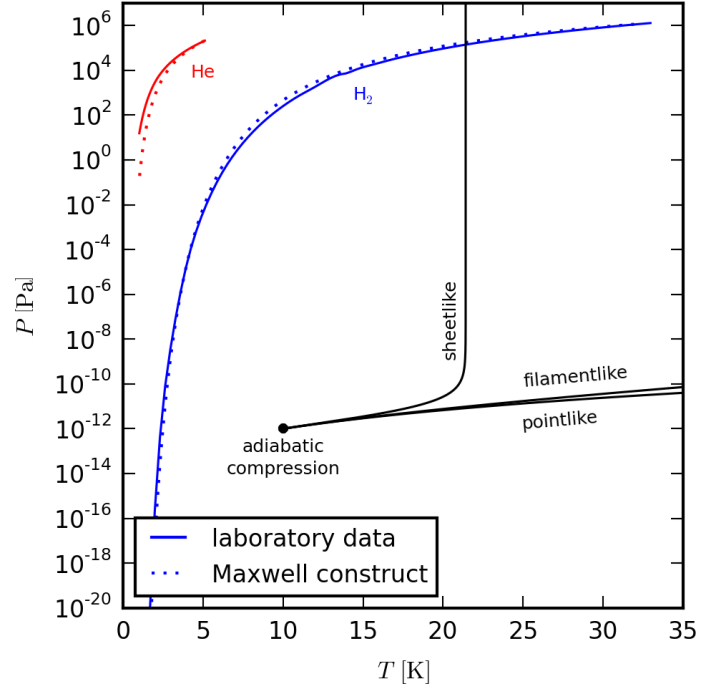


Fig. 2: H<sub>2</sub> and He laboratory data and van der Waals vapour curve derived from Maxwell construct. Adiabatic compression curves of an initial sphere to sheet-, filament- and point-like geometries for interstellar conditions ( $T = 10$  K,  $P = 10^{-12}$  Pa) are shown, as explained in Appendix B. Sheet-like collapses are allowed to reach the phase transition regime even without cooling. Cooling would displace the curves to lower temperature.

In addition, as shown in App. B.1, the adiabatic matter compression of a sheet-like geometry leads to a finite increase of potential energy, leading to a maximum relative temperature increase of only 2.1, while the energy diverges logarithmically in a filament-like geometry and as  $Z^{1/3}$  in a point-like geometry, where  $Z = \rho_{\text{final}}/\rho_{\text{initial}}$  is the density compression. This can be seen in Fig. 2 which shows how a sphere moves in this diagram when adiabatically compressed towards a sheet, filament, or point initially in interstellar conditions ( $T = 10$  K,  $P = 10^{-12}$  Pa). Whereas the temperature is quickly increasing with filament- and point-like geometries, in the sheet-like geometry it only rises to  $\sim 21$  K, which is well below the 33 K critical temperature of H<sub>2</sub>.

When taking radiative cooling into account, the temperature increase by contraction is even smaller. In App. B.2 we show that the opacity of a sheet-like collapse is barely increasing. If the initial medium is transparent, the final sheet is also transparent. On the other hand, in filament- and point-like collapses the opacity increases approximately as a power 1/2 or 2/3 of compression, quickly reaching a full opacity regime able to stop the collapse.

### 2.3. Lennard-Jones mixtures

The Jeans instability of Equ. (2) requires thermal equilibrium and is simplified by only considering linear perturbations. It does not predict its non-linear evolution when unstable. This is a motive to use molecular dynamical simulations with a Lennard-Jones potential in addition to gravity for studying such non-linear phenomena.

The Lennard-Jones potential

$$\Phi_{\text{LJ}}(r) = 4 \frac{\epsilon}{m} \left[ \left( \frac{\sigma}{r} \right)^{12} - \left( \frac{\sigma}{r} \right)^6 \right] \quad (9)$$

reproduces the van der Waals equation of state when in equilibrium conditions using the following relations (Caillol 1998):

$$T_c = 1.326 \frac{\epsilon}{k_B}, \quad (10)$$

$$n_c = 0.316 \sigma^{-3}, \quad (11)$$

$$P_c = 0.157 \frac{\epsilon}{k_B \sigma^3}. \quad (12)$$

For a fluid mixture, we use the usual Lorentz-Berthelot combining rule for the Lennard-Jones potential between two molecules

$$\Phi_{\text{LJ}}(r_{ij}) = 4 \frac{\epsilon_{ij}}{m_i} \left[ \left( \frac{\sigma_{ij}}{r_{ij}} \right)^{12} - \left( \frac{\sigma_{ij}}{r_{ij}} \right)^6 \right], \quad (13)$$

where  $\sigma_{ij} = \frac{1}{2}(\sigma_i + \sigma_j)$  and  $\epsilon_{ij} = \sqrt{\epsilon_i \epsilon_j}$  (Lorentz 1881; Berthelot 1898). The most accurate mixing rules for energy and distance are (Banaszak et al. 1995; Chen et al. 2001)

$$\sigma^3 = \sum_i^K \sum_j^K x_i x_j \sigma_{ij}^3, \quad (14)$$

$$\epsilon = \frac{\sum_i^K \sum_j^K x_i x_j \epsilon_{ij} \sigma_{ij}^3}{\sigma^3}. \quad (15)$$

Since  $T_c \propto \epsilon$  and  $n_c \propto \sigma^{-3}$ , we have  $n_c/n_{c,\alpha} = (\sigma/\sigma_\alpha)^{-3}$  and  $T_c/T_{c,\alpha} = \epsilon/\epsilon_\alpha$ . Using Equ. (7), we find  $P_c = (8/3)T_c n_c$ , and therefore  $P_c/P_{c,\alpha} = (\sigma/\sigma_\alpha)^{-3} \cdot (\epsilon/\epsilon_\alpha)$ .

As in the ideal gas case, using these mixing properties to calculate  $k_I$  in analogy to Equ. (1) instead of using Equ. (2) would lead to different results. In the ideal gas case, the biggest difference is  $\sim 10\%$ , but in the present case of a van der Waals fluid the difference can be much bigger, for example  $k_I$  always returns a finite number if the critical temperature of the mixture  $T_c > 1$ , whereas  $k_{\text{GZ}}$  can nevertheless be infinite if one of the components is in a phase transition.

### 2.3.1. Binary mixture

Considering a fluid consisting of two components  $\alpha$  and  $\beta$ , we define

$$\theta = \frac{T_{c,\beta}}{T_{c,\alpha}} = \frac{\epsilon_\beta}{\epsilon_\alpha}, \quad (16)$$

$$\nu = \frac{n_{c,\beta}}{n_{c,\alpha}} = \left( \frac{\sigma_\beta}{\sigma_\alpha} \right)^{-3}, \quad (17)$$

$$\mu = \frac{m_\beta}{m_\alpha}. \quad (18)$$

The following Lennard-Jones properties can be derived using Equ. (13 – 18):

$$\sigma_{\alpha\beta} = \frac{1}{2} \sigma_\alpha (1 + \nu^{-1/3}), \quad (19)$$

$$\epsilon_{\alpha\beta} = \epsilon_\alpha \theta^{1/2}, \quad (20)$$

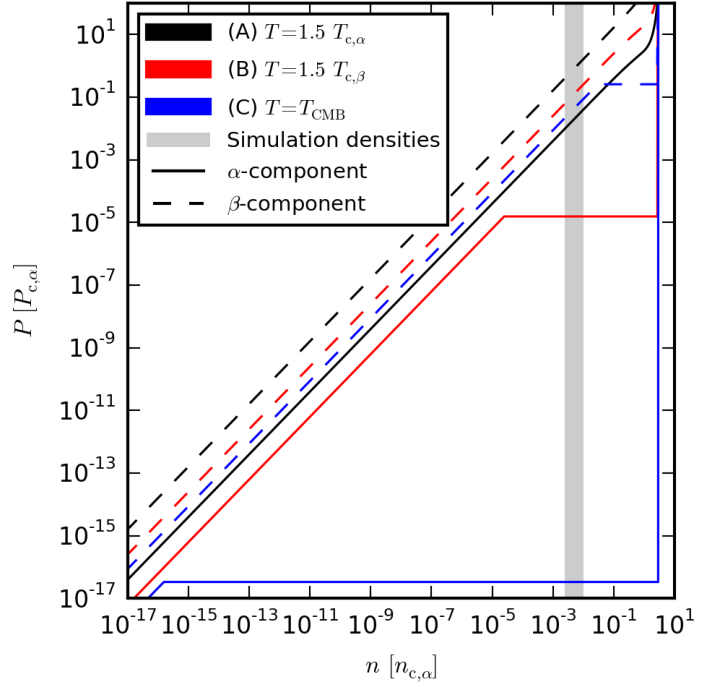


Fig. 3: van der Waals phase diagram with Maxwell construct for the  $\text{H}_2 - \text{He}$  mixture, each species considered as independent.

and the following van der Waals mixture properties:

$$\frac{n_{c,x}}{n_{c,\alpha}} = \left[ x_\alpha^2 + \frac{x_\alpha x_\beta}{4} (1 + \nu^{-1/3})^3 + \frac{x_\beta^2}{\nu} \right]^{-1}, \quad (21)$$

$$\frac{T_{c,x}}{T_{c,\alpha}} = \frac{n_{c,x}}{n_{c,\alpha}} \left[ x_\alpha^2 \nu^{1/3} + \frac{x_\alpha x_\beta \theta^{1/2}}{4} (1 + \nu^{-1/3})^3 + \frac{x_\beta^2 \theta}{\nu} \right], \quad (22)$$

$$\frac{P_{c,x}}{P_{c,\alpha}} = \frac{n_{c,x}}{n_{c,\alpha}} \cdot \frac{T_{c,x}}{T_{c,\alpha}}, \quad (23)$$

where  $x_\beta = 1 - x_\alpha$ . Without loss of generality we choose  $\theta < 1$ .

Three different cases can be distinguished, as shown in Fig. 3:

- (A)  $T_{c,\beta} < T_{c,\alpha} < T$   
Having the temperature above both critical values, neither component can be in a phase transition and  $k_{\text{GZ}}$  is always finite.
- (B)  $T_{c,\beta} < T < T_{c,\alpha}$   
 $\beta$  is still above the critical temperature and cannot be in a phase transition, but  $\alpha$  may or may not be in a phase transition depending on  $n_\alpha$ .
- (C)  $T < T_{c,\beta} < T_{c,\alpha}$   
Having the temperature below both critical temperatures, both components can be in a phase transition. At equal component number density,  $\alpha$  is faster in a phase transition, but theoretically, at low  $n_\beta$ ,  $\beta$  could be in a phase transition without  $\alpha$ , but this hardly ever happens in reality.

These three cases are studied using computer simulations (see Table 1).

### 2.3.2. Hydrogen-helium mixture

The critical temperature of  $\text{H}_2$  and  $\text{He}$  are 32.97 and 5.19K, whereas their usual Lennard-Jones  $\epsilon$  values are 36.4 and



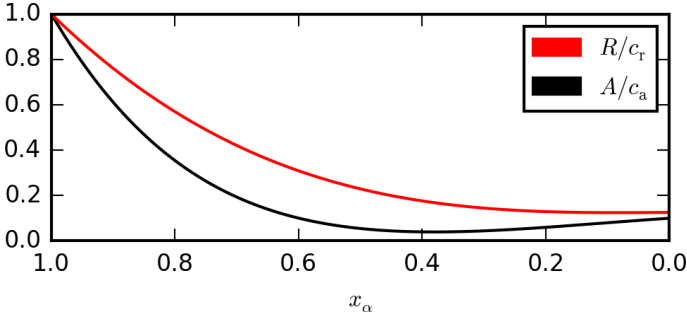


Fig. 4:  $R/c_r$  and  $A/c_a$  values as a function of  $x_\alpha$  for a H<sub>2</sub>-He mixture.

10.57  $k_B$  K. This is in conflict with the temperature conversion of Equ. (16), as  $\theta_{\text{H}_2\text{-He}} = 6.35$  using critical temperatures whereas  $\theta_{\text{H}_2\text{-He}} = 3.44$  using the Lennard-Jones  $\epsilon$  values. The same is the case to a lesser degree for the critical density.

All performed simulations are molecule independent, but  $\theta$ ,  $\nu$ , and  $\mu$  need to be defined. These values were set using  $T_c$ ,  $n_c$ , and the molecular mass of laboratory He and H<sub>2</sub> data (Air Liquide 1976). The goal of this article is to understand the role of a secondary component in a fluid presenting a phase transition together with gravity. In molecular clouds, the most likely case of a phase transition is  $T_{c,\text{H}_2} > T > T_{c,\text{He}}$ , thus it is important to have a correct  $(T_{c,\text{He}}/T_{c,\text{H}_2})$  fraction.

### 2.3.3. Virial theorem

In FP2015, the Lennard-Jones potential has been decomposed in attractive and repulsive terms:  $\Phi_{\text{LJ}} = \Phi_a + \Phi_r$ . In a binary mixture, we have to further distinguish the one-component terms  $\Phi_{\alpha^2}$  and  $\Phi_{\beta^2}$ , and the cross-terms  $\Phi_{\alpha\beta}$  and  $\Phi_{\beta\alpha}$  (see Equ. 13).

In analogy with Equ. (5) of FP2015, the virial theorem becomes as follows:

$$0 = \underbrace{2E_{\text{kin}} + 12E_r}_{>0} + \underbrace{6E_a + E_G}_{<0}. \quad (24)$$

There are two negative, attractive terms, and two positive, repulsive terms. If the attractive and repulsive terms equalize each other, the system is in virial equilibrium.

In the case of a homogeneous density and species distribution of mass  $M$ , the energy terms are

$$E_{\text{kin}} = \frac{3k_B T}{2m} M, \quad (25)$$

$$E_r = R \frac{\epsilon_\alpha \sigma_\alpha^{12} n^4}{m} M, \quad (26)$$

$$E_a = -A \frac{\epsilon_\alpha \sigma_\alpha^6 n^2}{m} M, \quad (27)$$

$$E_G = -G f_G(n, m) M^{5/2}, \quad (28)$$

with  $f_G > 0$  depending on the geometry. The repulsive and attractive constants are

$$R = c_r \left[ x_\alpha^5 + \theta \nu^{-4} x_\beta^5 + \frac{\theta^{1/2}}{2^{12}} (1 + \nu^{-1/3})^{12} (x_\alpha x_\beta^4 + x_\alpha^4 x_\beta) \right] \quad (29)$$

$$A = c_a \left[ x_\alpha^3 + \theta \nu^{-2} x_\beta^3 + \frac{\theta^{1/2}}{2^6} (1 + \nu^{-1/3})^6 (x_\alpha x_\beta^2 + x_\alpha^2 x_\beta) \right] \quad (30)$$

where the lattice coefficients  $c_r$  and  $c_a$  depend on the specific crystal lattice (FP2015), which are of importance for the solid

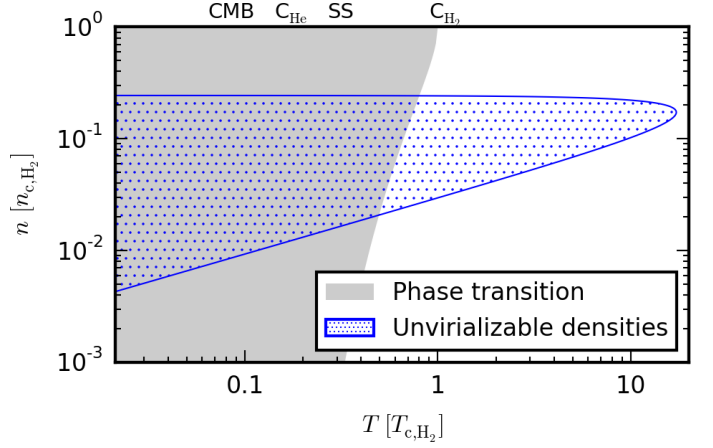


Fig. 5: van der Waals phase transition and unvirializable density for a binary mixture with  $x_\alpha = 0.75$ .

phase. Figure 4 shows  $R$  and  $A$  as functions of an abundance number fraction.

The above terms are for a fluid with no spatial separation of the species, i.e. a fluid in its initial state. The terms predict how an unstable fluid evolves. However, once a phase transition or a gravitational collapse happens, the species may separate. In that case, the terms have to be calculated for each species independently, using  $x_\alpha = 1$  and 0, respectively.

### 2.3.4. Unvirializable densities

The sum of the Lennard-Jones and kinetic terms must be positive as the gravitational term is negative:  $E_G < 0 < E_r + E_a + E_{\text{kin}}$ . This is the case if

$$2A\epsilon_\alpha (\sigma_\alpha^3 n)^2 \leq k_B T + 4R\epsilon_\alpha (\sigma_\alpha^3 n)^4. \quad (31)$$

There can be no virial equilibrium for any mass  $M > 0$ , if the attractive Lennard-Jones term dominates the kinetic and repulsive terms. We define the unvirializable density domain as follows:

$$\begin{aligned} \mathcal{D} &\equiv \{n : n_- < n < n_+\} \\ n_\pm^2 &= \sigma^{-6} \frac{1 \pm \sqrt{1 - 4 \frac{R}{A^2} \frac{k_B T}{\epsilon}}}{4 \frac{R}{A}}. \end{aligned} \quad (32)$$

If the term in the square root is negative, there is no real solution and therefore no unvirializable densities. This is the case if

$$T > T_{\text{max}} \equiv \frac{A^2}{4R} \frac{\epsilon}{k_B}. \quad (33)$$

Figure 5 shows the  $n_\pm$  values and the domain of the van der Waals phase transition for H<sub>2</sub>-He mixtures with a molecular fraction of  $x_\alpha = 0.75$ . There are unvirializable densities above the critical temperature  $T_c$  up to  $T_{\text{max}}$  even though no phase transition is possible.

The domain of phase transition does not change a lot for the different  $x_{\text{H}_2} > 0$ , as the H<sub>2</sub> phase transition temperature remains the same and the density changes as  $n_x = x \cdot n$ . It is at much lower temperatures for  $x_{\text{H}_2} = 0$ , as there is no H<sub>2</sub> anymore and the phase transition domain switches to He.

The evolution of fluids with unvirializable densities depends whether they are in a phase transition or not. If these fluids are in a phase transition, there is a gravitational instability independent of  $M$  (see 2.1.2), which leads to a collapse and the formation of

bodies of small mass. If they are not in a phase transition, there is only a gravitational collapse above a certain mass  $M$  (see Equ. 2). Below that mass, clumps form, which leads to an augmentation of the kinetic and repulsive Lennard-Jones terms until Equ. (31) is fulfilled, at which point an equilibrium is reached and the fluid may remain stable.

### 2.3.5. Dynamical friction

When discussing gravitational collapses, the concept of dynamical friction (Chandrasekhar 1943) is important, since heavy objects may condensate from the gas and start to precipitate, i.e. move with respect to the gas in the local gravity field. Considering a uniform density and Maxwellian velocity distribution, the dynamical friction of a heavy object of mass  $m_h$  reads

$$\frac{dv_h}{dt} = -\frac{4\pi G^2 m_h \rho \log(\Lambda)}{v_h^3} \left[ \text{erf}(X) - \frac{2X}{\sqrt{\pi}} \exp(-X^2) \right] v_h, \quad (34)$$

where  $\log(\Lambda)$  is the Coulomb logarithm and  $X = v_h / \sqrt{2\sigma_v}$ . For the qualitative analysis needed in this work, it is enough to state

$$\frac{dv_h}{dt} \propto -m_h. \quad (35)$$

This can be used in different cases. First, He is twice as heavy as  $H_2$  and can therefore be considered a heavy object and in some conditions lead to sediment faster than  $H_2$ . Secondly, when  $H_2$  is in a phase transition,  $H_2$  ice grains may sediment faster than He.

## 3. Method

For all of the simulations, the Large-Scale Atomic/Molecular Massively Parallel Simulator (LAMMPS) is used (Plimpton 1995). The use of its short-range Lennard-Jones solver and long-range gravitational solver, super-molecules, and the rRESPA time integrator are discussed in FP2015.

We recall the following super-molecule properties, where  $\eta$  is the number of molecules per super-molecule,

$$m_{SM} = \eta m, \quad (36)$$

$$\epsilon_{SM} = \eta \epsilon, \quad (37)$$

$$\sigma_{SM} = \eta^{1/3} \sigma, \quad (38)$$

where  $m$ ,  $\sigma$ , and  $\epsilon$  are the values for one molecule. The gravitational constant, described in molecular dynamics units ( $\sigma = \epsilon = m = 1$ ), is

$$G_{SM} = \frac{Gm^2}{\sigma\epsilon} \eta^{2/3}. \quad (39)$$

In order for the gravitational force between two super-molecules to be consistently small compared to the intermolecular forces,  $\eta$  should satisfy the following constraint:

$$\eta^{2/3} \ll \frac{24\epsilon\sigma}{Gm^2} (r_c^{-5} - 2r_c^{-11}), \quad (40)$$

where  $r_c$  is the cut-off radius in  $\sigma$  units (set to  $r_c = 4$  in the simulations).

Two molecules are considered as bound in LAMMPS if their distance is smaller than  $1.3625\sigma$ . A clump of bound molecules can be either gaseous or condensed, dependent whether its temperature is above or below the critical value.

Initially, the fluid is uniformly distributed in a periodic cubic box. To reproduce the most generic plane-parallel collapse

first, as explained in Sect. 2.2, a velocity perturbation in form of a small plane sinusoidal wave in the  $x$  direction is superposed to the fluid's Maxwellian velocity distribution. The perturbation strength is of 1%; see FP2015 for how the perturbation is calculated.

### 3.1. Units

All simulations are performed in dimensionless units and only the ratios of physical quantities matter. The initial properties of a fluid are the ratios of its temperature to the critical value  $T_c$ , its number density to the critical value  $n_c$ , the Lennard-Jones constant ratios  $\theta$ ,  $\nu$ , the mass ratio  $\mu$ , the molecular fraction  $x_\alpha$  and the gravitational potential strength  $\gamma_G$ . The needed molecule parameters were set in accordance to laboratory  $H_2$  and He values

$$\theta = \frac{T_{c,He}}{T_{c,H_2}} = 0.157, \quad (41)$$

$$\nu = \frac{n_{c,He}}{n_{c,H_2}} = 1.12, \quad (42)$$

$$\mu = \frac{m_{He}}{m_{H_2}} = 2. \quad (43)$$

The time unit is defined as the particle crossing time for the box of length  $L$ , i.e.

$$\tau = \frac{L}{V}, \quad (44)$$

where  $V^2 = 3Nk_B T / \sum_i m_i$ ,  $i = 1 \dots N$ .

The gravitational constant strength is measured by a factor  $\gamma_J$  relative to the ideal gas Jeans limit strength  $G_J$ , defined as

$$\gamma_J = \frac{G}{G_J}, \quad (45)$$

$$G_J = \frac{\pi\gamma k_B T}{L^2 \sum_{j=\alpha,\beta} n_j m_j^2}.$$

### 3.2. Visualization

In order to visualize the particle snapshots, two-dimensional number density maps are used. The introduced perturbation is along the  $x$ -axis, thus the sheet-like collapse is parallel to the  $yz$ -plane. For that reason, the density map shows the  $y$ - and  $z$ -axes where most of the relevant events can be observed. When showing all  $N$  particles, smaller aggregates are washed out and barely visible, which is why only a slice of the whole simulation box is shown. Figure 6 shows how this slice is selected: The highest number density is determined in the  $x$  direction in order to be centred around the collapse region. From there, the slice width  $\Delta x$  is calculated in order to contain  $N_{\text{slice}} = f_{\text{slice}} N$  particles. In that way, the slice width  $\Delta x$  differs for every snapshot, but always contains the same number  $N_{\text{slice}}$  of particles.

The number density  $n$  and number fraction  $x_\alpha$  are represented by brightness and colour. As at low density the brightness is maximum and the colour is simply white, the colour map is best visualized in polar coordinates, where  $n$  is the radius and  $x_\alpha$  the angle. Figure 7 shows the colour map used, for better contrasts, the brightness is represented in logarithmic scale.

## 4. Simulations

In FP2015, we simulated fluids with only one component. We introduced the terms comets for clumps that are principally bound

Table 1: Simulation parameters

Name	$x_\alpha$	$n$		$T$		$\gamma_J$	$N_{\text{tot}}$	$M_{\text{tot}}/M_\oplus^{a,b}$		$L/R_\oplus^{a,b}$		$\tau/\text{kys}^a$	
		$[n_{c,\alpha}]$	$[\text{m}^{-3}]^a$	$[T_{c,\alpha}]$	$[\text{K}]^a$			(f)	(g)	(f)	(g)	(f)	(g)
A10	1.0	$10^{-2}$	$9.3 \cdot 10^{25}$	1.5	49.5	0, 0.5, 1.5	$100^3$	0.34	1.7	27	47	0.86	1.5
A75	0.75							0.094	0.49	16	28	0.58	1.0
A50	0.5							0.039	0.2	11	20	0.45	0.78
A25	0.25							0.019	0.1	8.6	15	0.36	0.64
A00	0.0							0.011	0.056	6.8	12	0.31	0.53
A75 <sub>s</sub>	0.75	$10^{-2}$	$9.3 \cdot 10^{25}$	1.5	49.5	1.5	$50^3 - 160^3$	0.49		18		1.0	
A75 <sub>01</sub>		$10^{-1}$	$9.3 \cdot 10^{26}$					0.16		9		0.29	
B10	1.0	$10^{-2}$	$9.3 \cdot 10^{25}$	0.24	7.8 <sup>c</sup>	0, 0.5, 1.5	$80^3$	0.021	0.11	11	18	0.86	1.5
B75	0.75							0.0059	0.031	6.5	11	0.58	1.0
B50	0.5							0.0024	0.013	4.5	7.9	0.45	0.78
B25	0.25							0.0011	0.0063	3.4	5.9	0.36	0.63
B00	0.0							0.00068	0.0035	2.7	4.7	0.31	0.53
B75 <sub>y</sub>	0.75	$10^{-2}$	$9.3 \cdot 10^{25}$	0.24	7.8	0.5 – 1.5	$80^3$	0.0059 – 0.031		6.5 – 11		0.58 – 1.0	
B75 <sub>01</sub>		$10^{-1}$	$9.3 \cdot 10^{26}$					0.0097		3.6		0.32	
C10	1.0	$10^{-2}$	$9.3 \cdot 10^{25}$	0.082	2.7 <sup>d</sup>	0, 0.5, 1.5	$80^3$	0.0043	0.022	6.3	11	1.5	0.86
C75	0.75							0.0012	0.0063	3.8	6.6	1.0	0.58
C50	0.5							0.00049	0.0026	2.7	4.6	0.78	0.45
C25	0.25							0.00025	0.0013	2.0	3.5	0.63	0.36
C00	0.0							0.00014	0.00072	1.6	2.8	0.53	0.31
SSM <sub>01</sub>	0.84	$10^{-1}$	$9.3 \cdot 10^{26}$	0.3	10	1.05	$80^3$	0.012 <sup>e</sup>		3.9		0.3	
SSM <sub>02</sub>		$10^{-2}$	$9.3 \cdot 10^{25}$					0.012 <sup>e</sup>		8.5		0.65	
SSE <sub>04</sub>		$10^{-4}$	$9.3 \cdot 10^{23}$					1.0		171		13	

**Notes.** All simulations are initially perturbed by a small plane sinusoidal wave in the  $x$ -direction as in FP2015.

<sup>(a)</sup> Considering  $\alpha = \text{H}_2$  and  $\beta = \text{He}$ . <sup>(b)</sup>  $\oplus \equiv \text{Earth}$  <sup>(c)</sup>  $T = 1.5T_{c,\text{He}}$ . <sup>(d)</sup>  $T = T_{\text{CMB}}$ . <sup>(e)</sup>  $M = M_{\text{Moon}}$ . <sup>(f)</sup>  $\gamma_J = 0.5$ . <sup>(g)</sup>  $\gamma_J = 1.5$ .

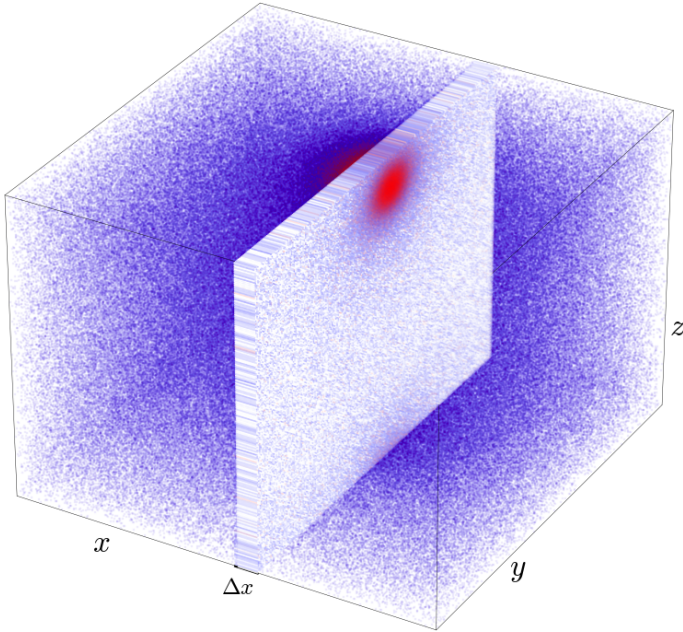


Fig. 6: Two-dimensional density map of three-dimensional space.

by the Lennard-Jones potential and planetoids for clumps that are principally bound by gravity. If a fluid is in a phase transition, it is important to distinguish between a strong gravitational potential above the ideal gas Jeans criterion and a weak grav-

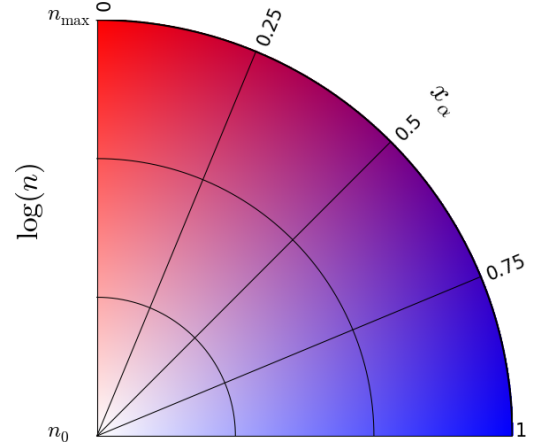


Fig. 7: Colour mapping of density map.

itational potential below it. In the strong gravity case, a gravitational collapse happens, leading to the formation of a hot, gaseous planetoid. Phase transitions only happen at the beginning as the fluid heats up above the critical temperature where no solid comets can form.

In the weak gravity case, no gravitational collapse happens and solid comets form thanks to the phase transition. The comets attract each other gravitationally, which leads to the formation of a solid planetoid. During the comet aggregation, the number of bound molecules does not rise. This means that the planetoid only captures comets and no single molecules. Therefore,

the fraction of bound molecules is identical to the number of molecules that underwent phase transition.

In this article, we compare fluids with different molecular fractions by keeping the physical properties alike (constant  $T/T_{c,\alpha}$  and  $n/n_{c,\alpha}$ ). By decreasing  $x_\alpha$  the mean mass per molecule  $m$  increases, since  $m_\alpha < m_\beta$ . It is therefore not possible to have the same number of molecules per super-molecule  $\eta$ , the same super-molecule mass  $M_{SM} = m\eta$ , and the same gravity  $G_J \propto m^2\eta^{2/3}$  at the same time.

Since we want to study the reaction of fluids with different  $x_\alpha$  above and below the ideal gas Jeans criterion, we need to ensure that  $\gamma_J$  is  $> 1$  or  $< 1$  in the compared simulations. For that reason, neither the total mass nor the number of molecules remains the same when comparing fluids with different  $x_\alpha$ , while  $\gamma_J$  remains the same. Since  $G \propto m^{-2}$  (Equ. 45) and  $\eta^{2/3} \propto m^{-2}G$  (Equ. 39), then  $\eta \propto m^{-6}$  and thus  $M = m\eta \propto m^{-5}$ . Therefore, changing  $m$  by a factor 2 leads to a total mass factor decrease of 32.

Different cases are studied:  $T = 1.5T_{c,\alpha}$ ,  $T = 1.5T_{c,\beta}$  and  $T = (T_{CMB}/T_{c,H_2})T_{c,\alpha}$  with  $n = 10^{-2}n_{c,\alpha}$  and  $x_\alpha = 1, 0.75, 0.5, 0.25$ , and 0. These initial parameters are shown in Fig. 3. In addition, different densities are used for simulations B75 and C75 to compare cases with  $n > n_-$  with  $n < n_-$  (see Sect. 2.3.3). We also study solar system abundances for different total masses and number densities. The simulations are summarized in Table 1.

The simulations with  $\gamma_J < 1$  were run until a steady-state solution was reached. Most simulations with  $\gamma_J > 1$  were stopped once a planetoid formed, which typically happens after  $\sim 5\tau$ . Even if the resulting fluid did not reach a steady state then, no further developments are expected, as checked in FP2015. A few simulations were run for  $15\tau$  to confirm this. At  $t = 5\tau$ , the planetoid of B75 with  $\gamma = 1.5$  is 15% hotter than average, whereas unbound molecules are 5% colder. After another  $10\tau$ , however, at  $t = 15\tau$ , the temperature differences are below 1%. Similarly, at  $t = 5\tau$ , there are very strong regional temperature differences of  $\geq 10\%$  considering subdomains of 1% volume. At  $t = 15\tau$ , they are  $\leq 5\%$ .

#### 4.1. Above critical temperatures

In this Section, we consider fluids where both  $T_\alpha$  and  $T_\beta$  are above the critical temperature. The number densities corresponding to the different abundance number fractions can be seen in Fig. 3.

##### 4.1.1. Time evolution

Figure 8 shows the global temperature evolution of the A simulations (see Table 1). In all simulations, the weakly self-gravitating fluids with  $\gamma_J = 0.5$  and the fluids without gravity are very similar and do not react significantly to the velocity perturbation. On the other hand, as expected for the sufficiently self-gravitating fluids with  $\gamma_J = 1.5$  the introduced perturbation rises exponentially. The reaction time is similar for all number fractions, but the mixtures reach slightly higher temperatures. Keeping in mind that all simulations have the same  $\gamma_J$  value, but the total mass differs with  $M_1/M_2 = (m_1/m_2)^{-5}$ .

To get a deeper understanding of the internal processes, we need to distinguish between the  $\alpha$  and  $\beta$  component. Figure 9A shows the fraction of bound molecules in the simulations as a function of time. No phase transition happens above the critical temperature, therefore no comets form in the simulations with  $\gamma_J = 0$  and 0.5. With  $\gamma_J = 1.5$ , the gravitational collapse leads to

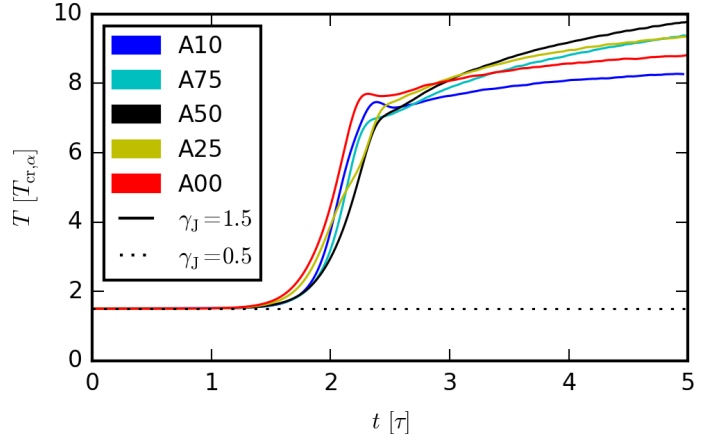


Fig. 8: Global temperature as a function of time of the A simulations with  $\gamma_J = 1.5$  and 0.5.

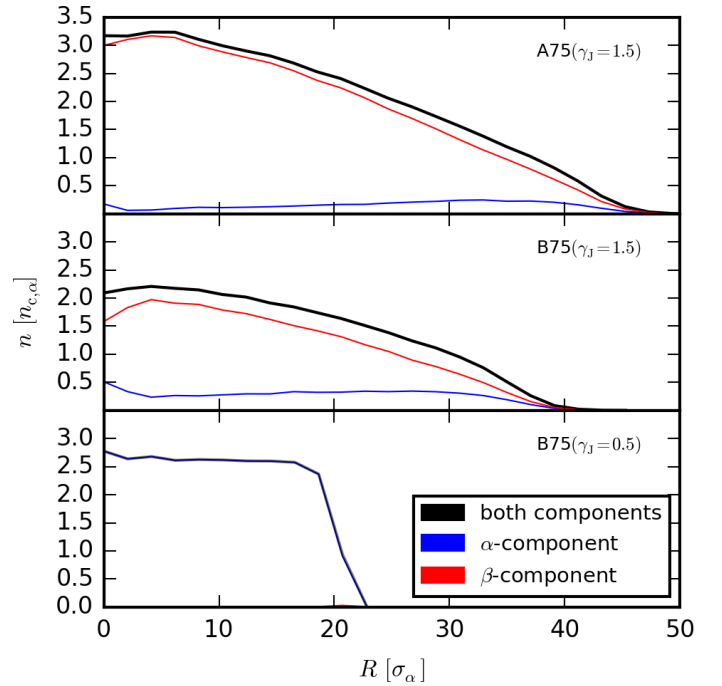


Fig. 11: Density of planetoid as a function of the radius of the simulations A75 and B75 with  $\gamma_J = 1.5$  at  $t = 5\tau$  and B75 with  $\gamma_J = 0.5$  at  $t = 30\tau$ .

the formation of a planetoid. In its centre, the gravitational pull is strong enough to keep the molecules bound even though the temperature is well above the critical value.

The  $\beta$ -molecules, as they are twice as heavy as the  $\alpha$ -molecules, fall faster into the forming planetoid. Indeed, even in A75, with only  $x_\beta = 0.25$ , the fraction of bound  $\beta$ -molecules surpasses the fraction of bound  $\alpha$ -molecules for  $\tau > 2$ .

##### 4.1.2. Planetoid formation

Figure 10a (page 20) shows a time sequence of snapshots and super-molecule, comet-size distributions condensed as grains or comets. The parameter  $N_{\text{comet}}$  is the number of super-molecules in one comet and  $f(N_B)$  is the comet size distribution function. At the beginning with  $t < 3\tau$ , small comets of either  $\alpha$ - or  $\beta$ -molecules form. At  $t = 3\tau$ , a planetoid with  $N \approx 0.1N_{\text{tot}}$  forms

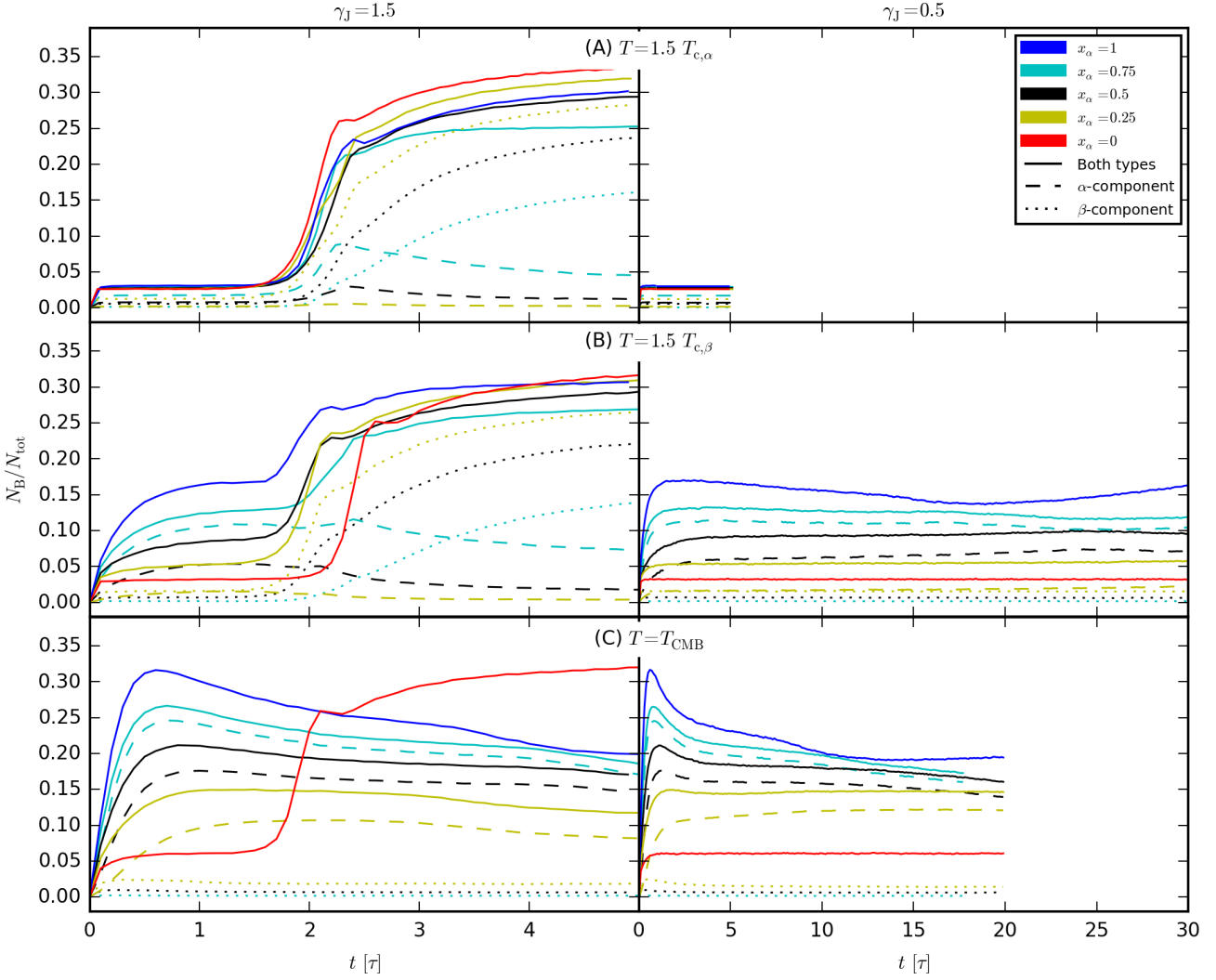


Fig. 9: Evolution of the number of bound molecules as a function of time of the A, B, and C simulations with  $\gamma_J = 1.5$  and  $0.5$ . The simulations with  $\gamma_J = 0.5$  are stopped after  $5\tau$ ,  $30\tau$ , and  $20\tau$  for the A, B, and C simulations, respectively, when no further significant development is expected.

consisting of both components. One can already see a dominance of  $\beta$ -molecules, especially in the centre.

Beginning at  $t = 3\tau$ , and even more clearly at  $t = 4\tau$ , one can observe the formation of a big core consisting only of  $\beta$ -molecules (isolated  $\beta$ -dot). In the snapshots this corresponds to the planetoid shown as a  $\beta$ -core surrounded by  $\alpha$ -molecules. Once the planetoid has reached this form, it reaches a steady state. Its temperature matches the gas temperature, and the temperature fluctuations level out (see FP2015 for more details on planetoid and comet temperatures).

Figure 11 (top) shows the planetoid density of simulation A75 as a function of radius. Even though the fluid consists of only 25%  $\beta$ -molecules, the planetoid consists mostly of  $\beta$ -molecules with  $f_\beta = 0.86$ . The  $\alpha$ -molecules are only a small fraction and mostly present in the outer part. The gaseous nature of this body is visible as the density regularly decreases in radii.

#### 4.1.3. Scaling

The scaling of simulations using super-molecules has already been discussed in FP2015. In order to obtain the correct behaviour, the gravitational forces  $F_G$  need to be small on inter-

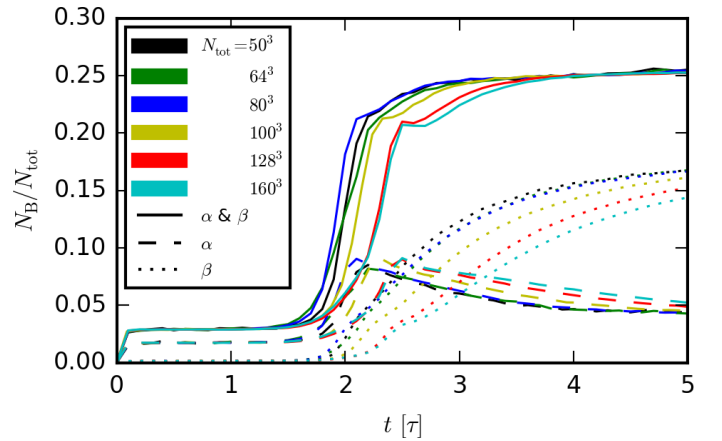


Fig. 12: Fraction of bound molecules as a function of time for the simulations A75<sub>S</sub> with  $\gamma_J = 1.5$  and different  $N_{\text{tot}}$ .

molecular scales compared to the Lennard-Jones forces  $F_{\text{LJ}}$ , i.e.  $F_G(r_c) < F_{\text{LJ}}(r_c)$ , where  $r_c$  is the cut-off radius (see Equ. 40). A turning point can be identified up to which  $N_B$  ( $N_{\text{comet}}$ ) follows



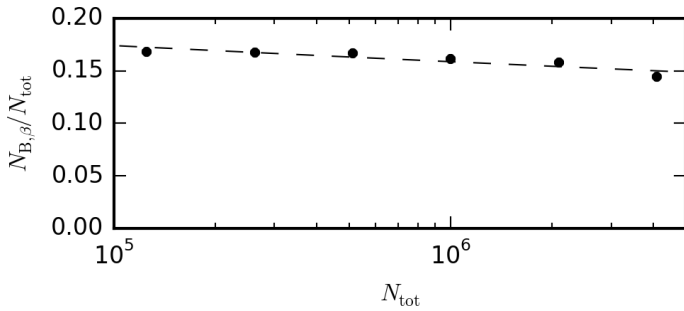


Fig. 13: Fraction of bound  $\beta$ -molecules as a function of  $N_{\text{tot}}$  for the simulations A75<sub>S</sub>.

the power-law  $N_B(N_{\text{comet}}) \propto N_{\text{comet}}^{\xi_c}$  with negative index  $\xi_c < -1$ , whereas after the turning point  $N_B(N_{\text{comet}})$  follows a second power law with index  $\xi_p = 1$  (see Fig. 10a). The appearance time of this turning point is independent of  $N_{\text{tot}}$ , whereas the size of the comet at the turning point scales as  $N_{\text{comet}}/N_{\text{tot}} \approx 10 N_{\text{tot}}^{-1}$ , thus  $N_{\text{comet}} \approx 10$ . This corresponds roughly to the smallest number of nearest neighbours in the condensed phase in 3D for which surface effects start to be dominated by volume effects.

Figure 12 shows the fraction of bound molecules as a function of time for all A75<sub>S</sub> simulations with  $N_{\text{tot}} = 50^3$  to  $160^3$ . As shown in FP2015, the slight time delay between the simulations can be attributed to the random seed. In any case, the asymptotic final value is physically more important, and is the same for all  $N_{\text{tot}}$  when considering both components. The final value of the  $\beta$ -molecules, on the other hand, very slightly declines with increasing  $N_{\text{tot}}$  as can be seen in Fig. 13. It follows the power-law  $N_B/N_{\text{tot}} \approx 0.213 N_{\text{tot}}^{-0.017}$  over the range  $N_{\text{tot}} = 10^5 - 10^{6.5}$ .

#### 4.1.4. Extrapolation to physical scale

The simulations should actually represent a  $\text{H}_2$ -He fluid mixture with  $\sim 10^{50}$  molecules. As outrageous as this extrapolation might appear, this is exactly what usually takes place in many other types of simulations (cosmological, galactic, or stellar simulations) because as long as the physical scale invariant aspect of the physics between the macro- and micro-scales are separated by enough orders of magnitude the exact range of scale difference does not matter over dynamical timescales. For longer simulation timescales one can check how the results scale with  $N$  by running simulations with different  $N$ , which is the reason why we always run the simulations with several  $N$ . Extrapolating the previous power law to physical scales, we find that  $\sim 3\%$  of  $\beta$ -molecules settle inside the planetoid, instead of  $\sim 15\%$ . Thus the simulations overestimate species segregation, which is to be expected in view of the increased fluctuations when the number of particles decreases. Segregation effects should be treated with caution, as we are extrapolating values in a range that is less than two orders of magnitude or 45 orders of magnitude away. Larger simulations should allow us to better constrain the effective species segregation in realistic conditions.

#### 4.2. Between critical temperatures

In this section, we consider fluids with  $T_\alpha < T_{c,\alpha}$  and  $T_\beta > T_{c,\beta}$  with different component fraction  $x_\alpha$ . The number density  $n$  has been chosen in such a way that for the molecular fractions  $x_\alpha > 0$ , the  $\alpha$ -component with number density  $n_\alpha = x_\alpha \cdot n$  is in a phase transition.

As the temperature of the B simulations is an order of magnitude smaller than in the A simulations, the same is the case for the gravitational potential (see Equ. 45). For that reason, it is sufficient to use  $N_{\text{tot}} = 80^3$  for these simulations.

##### 4.2.1. Above the ideal gas Jeans criterion

Figure 9B on the left side shows the time evolution of the fraction of bound molecules for the B simulations with  $\gamma_j = 1.5$ . One can see the similarity to Fig. 9A, but the fluids with a high  $x_\alpha$  value are rising to higher values even before the perturbation is becoming dominant. This is because the  $\alpha$ -portion of the fluid is in a phase transition and small ice grains are forming even without the help of gravity. The formed planetoid is gaseous, as can be seen in Fig. 11 (middle). This shows that the phase transition does not have an important effect if  $\gamma_j > 1$  and that the instability can be predicted by the ideal gas Jeans criterion.

The density at the core of the planetoid of simulation B75 is lower than that of A75. This is explained by the fact that by keeping  $\gamma_j = 1.5$ , the value for  $G_j$  is lower for the B simulations than for the A simulations as  $G_j \propto T$  (see Equ. 45). Having a lower gravitational potential, the density at which the repulsive Lennard-Jones term and the attractive gravitational term are equal is lower.

The planetoid is still dominated by  $\beta$ -molecules, but there are more  $\alpha$ -molecules than in the A75 simulation with  $f_\alpha = 0.26$  and  $f_\beta = 0.74$ . As in the A simulations, the core consists of gaseous He, as is clearly visible in Fig. 10b (page 20).

##### 4.2.2. Below the ideal gas Jeans criterion

As can be seen in Fig. 3, the  $\alpha$ -component of the simulations B10, B75, B50, and B25 all lie on the Maxwell line and are thus in a phase transition, which implies, according to Equ. (2), that they are gravitationally unstable even with  $\gamma_j < 1$ .

The right side of Figure 9B shows the evolution of the fraction of bound molecules of the B simulations with  $\gamma_j = 0.5$ . The timescale is much larger ( $30\tau$  instead of  $5\tau$  in the case of  $\gamma_j = 1.5$ ), having a smaller gravitational potential, the long-range gravitational term is lower, and therefore the creation of any potential comet or planetoid takes more time.

The one-component fluids, consisting of either uniquely  $\alpha$ -molecules (B10) or  $\beta$ -molecules (B00) have already been studied in detail in FP2015. The  $\alpha$ -fluid B10 is unstable as it is in a phase transition, whereas the  $\beta$ -fluid B00 is stable as its temperature is above the critical value and no phase transition is possible.

The simulations of fluid mixtures B25, B50, B75 with  $\gamma_j = 0.5$  are all unstable, even gravitationally. We can distinguish a clear difference in the simulations with  $\gamma_j = 1.5$  in that only the  $\alpha$ -molecules form comets, whereas the  $\beta$ -molecules remain in gaseous form. Even in the simulation B25, which has only 25%  $\alpha$ -molecules, the comets and planetoid consist almost exclusively of  $\alpha$ -molecules. This difference between  $\gamma_j = 1.5$  and 0.5 can also be seen when comparing Fig. 14a with Fig. 10b (pages 21 and 20).

Figure 11 (bottom) shows the radius of the planetoid at  $t = 30\tau$  of B75 with  $\gamma_j = 0.5$ . Comparing with the planetoid of B75 with  $\gamma_j = 1.5$ , we see that the high-gravity planetoid consists mostly of  $\beta$ -molecules in gas phase, whereas the low-gravity planetoid consists of mostly  $\alpha$ -molecules in solid phase, surrounded by an atmosphere. Very few  $\beta$ -molecules have been trapped during the planetoid formation, providing an interesting

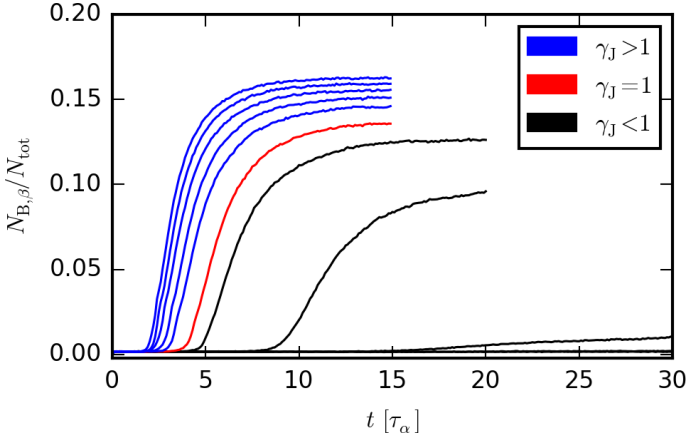


Fig. 15: Fraction of bound  $\beta$ -molecules as a function of time for the simulations B75 <sub>$\gamma$</sub> . The simulations are stopped once they reach asymptotic values.

example of a body forming with a distinct composition from the original medium as a result of the initial phase transition state.

#### 4.2.3. Different $\gamma_J$ values

The previous sections show that a fluid in a phase transition above the ideal gas Jeans criterion, i.e. with  $\gamma_J = 1.5$ , forms a gaseous planetoid consisting mostly of  $\beta$ -molecules due to a classical ideal gas Jeans collapse. On the other hand, a fluid in a phase transition with  $\gamma_J = 0.5$  forms small  $\alpha$ -comets due to the phase transition. These comets are attracted to each other by gravity, leading to the formation of a rocky planetoid, consisting almost exclusively of  $\alpha$ -molecules. In this section, we vary  $\gamma_J$  from 0.5 to 1.5.

Figure 15 shows the fraction of bound  $\beta$ -molecules. It is rising steeply for fluids with  $\gamma_J > 1$  in accordance with the ideal gas Jeans criterion and the formed planetoid is gaseous and consists mostly of  $\beta$ -molecules. The fluid with  $\gamma_J = 1$  also produces a gaseous planetoid, but the percentage of  $\beta$ -molecules is already dropping a little. Interestingly, in the fluids with  $0.7 \leq \gamma_J < 1$ , the  $\beta$  fraction is also rising. The instability criterion of Equ. (2) is for all components, not only one of them.

Figure 14b (page 21) shows snapshots and comet-size distributions of simulation B75 <sub>$\gamma$</sub>  with  $\gamma_J = 0.8$ . One sees that at first ( $t \leq 8\tau$ ) only the  $\alpha$ -molecules are collapsing and forming a rocky planetoid. Then, owing to the great attractive force of the  $\alpha$ -planetoid, many  $\beta$ -molecules gather around it, forming an atmosphere ( $t = 12\tau$ ). A  $\beta$ -atmosphere can also be observed, in a less striking way, for the simulation with  $\gamma_J = 0.5$  in Fig. 14a. What happens afterwards is very interesting: at  $t = 16\tau$ , one sees that the rocky planetoid swaps the  $\alpha$ - and  $\beta$ -molecules and the heavier  $\beta$ -molecules replace the  $\alpha$ -molecules near the centre.

#### 4.3. Below critical temperatures

In this Section, to complete the study of binary fluid mixtures, we consider fluids where both  $T_\alpha$  and  $T_\beta$  are below the critical temperature. The number density  $n$  has been chosen in such a way that for the molecular fractions  $x_\alpha > 0$ , the  $\alpha$ -component with number density  $n_\alpha = x_\alpha \cdot n$  is in a phase transition.

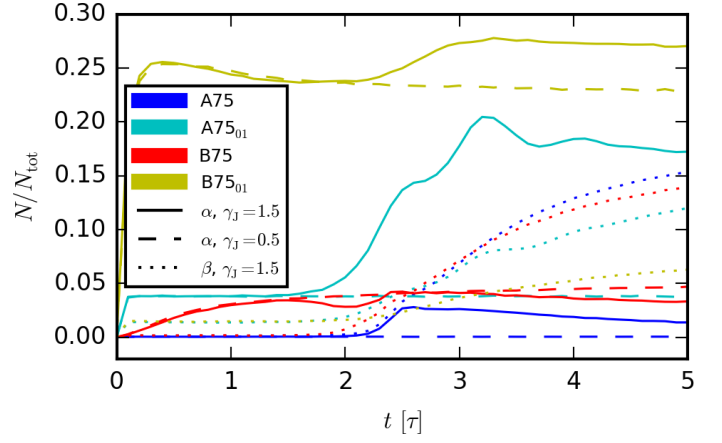


Fig. 17: Fraction of bound molecules with cluster mass  $m_{cl} > m_{He}$  as a function of time of simulations in and out of the unvirializable density domain.

##### 4.3.1. Above the ideal gas Jeans criterion

The left side of Figure 9C (page 9) shows the time evolution of bound molecules of the C simulations with  $\gamma_J = 1.5$ . There is a distinct difference compared to the A and B simulations, which form  $\beta$ -planetoids; only the percentage of bound  $\alpha$ -molecules rises and the forming planetoid only consists of  $\alpha$ -molecules (see Fig. 16, page 22). This is slightly counter-intuitive at first, as one could expect the  $\beta$ -molecules to be even more eager to fall into the planetoid than in the A and B simulations, since the temperature is lower.

Owing to the very low temperature of the C-simulation, however, the  $\alpha$ -molecules quickly form comets from the very beginning. These comets are heavier than the  $\beta$ -molecules and decelerate faster into the planetoid.

##### 4.3.2. Below the ideal Gas Jeans criterion

The evolution of the simulations below the ideal gas Jeans criterion is analogous to the B simulations. The fraction of bound  $\alpha$ -molecules in the pure  $\alpha$ -fluid and the mixture rise, and the fraction of bound molecules of the pure  $\beta$ -fluid remains very low. This is in accordance with Fig. 3 where the  $\alpha$ -molecules are unstable but the  $\beta$ -molecules are stable. The simulations C10, C75, C50, and C25 form a rocky  $\alpha$ -planetoid, as already seen in the B simulations (see Fig. 14a).

#### 4.4. Virial theorem

When comparing the simulations above the ideal gas Jeans instability, there is a clear difference between the A and B simulations on one side, and the C simulations on the other. A gaseous  $\beta$ -planetoid forms in the first two, whereas a rocky  $\alpha$ -planetoid forms in the latter. Looking at the virial terms of the fluids (see Sec. 2.3.3), Equ. (31) is fulfilled in the A and B simulations, whereas for the C simulation, the density is in the unvirializable domain  $\mathcal{D}$ . In this Section, we vary the densities of the A and B simulations in order to be in and out of the unvirializable domain.

Figure 17 shows the time evolution of clusters that have a higher mass than one  $\beta$ -molecule ( $N_{cl,\alpha} > 2$ ) for the simulations in the unvirializable domain (A75<sub>01</sub> and B75<sub>01</sub>) and below (A75 and B75). A very quick rise of H<sub>2</sub> comets for the unvirializable fluid happens, both with and without gravity, which is in ac-

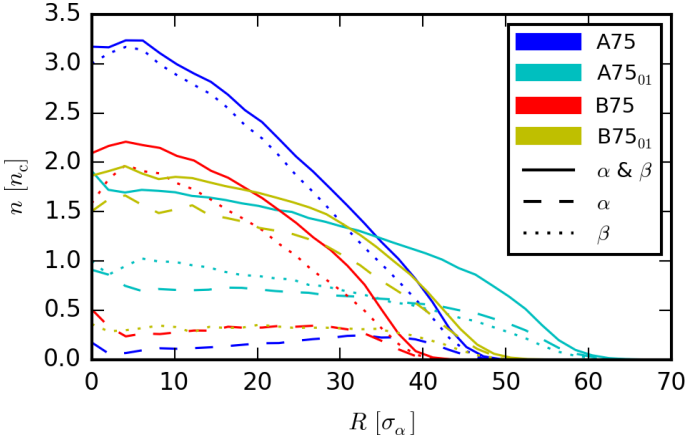


Fig. 18: Density of planetoid at  $t = 5\tau$  as a function of the radius of the simulations in and out of the unvirializable density domain.

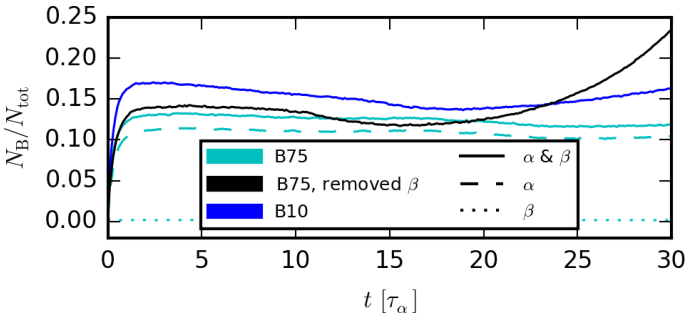


Fig. 19: Fraction of bound molecules as a function of time of the simulations B75, B75 with removed  $\beta$ -molecules and B10.  $\gamma_J = 0.5$ .

cordance with Equ. (31), as neither the repulsive Lennard-Jones term nor the kinetic energy can withhold the attractive Lennard-Jones term thus leading to the formation of comets. Even in simulation A75<sub>01</sub>, with a temperature above the critical temperature, this comet formation is taking place, even though a phase transition is officially not possible. A slow comet formation only takes place for the virializable fluids.

Once the exponential growth of the perturbation becomes important ( $t \geq 2\tau$ ), the unvirializable fluids have created an important number of comets heavier than the  $\beta$ -molecules, which fall faster in the forming planetoid as a result of dynamical friction. This can be seen in Fig. 18 where the planetoids of the simulations A75 and B75 consist mostly of  $\beta$ -molecules, whereas the planetoid of B75<sub>01</sub> consists mostly of  $\alpha$ -molecules. A somewhat special case is A75<sub>01</sub>, where the planetoids composition is almost perfectly fifty-fifty. This can be explained by the fact that because it is above the critical temperature, the comets are not really solid, but consist of a dense gas that is able to mix easily with  $\beta$ -molecules. Thus, once a  $\alpha$ -planetoid has formed using all the heavy  $\alpha$ -comets, the  $\beta$ -comets fall into the planetoid and mix with it.

#### 4.5. Influence of $\beta$ -molecules on $\alpha$ -molecules below the ideal gas Jeans criterion

As can be seen in Fig. 9C, almost no  $\beta$ -molecules form comets if  $\gamma_J = 0.5$  and the percentage of  $\beta$ -molecules in the planetoid is negligible. Granted, the concentration of He around the plan-

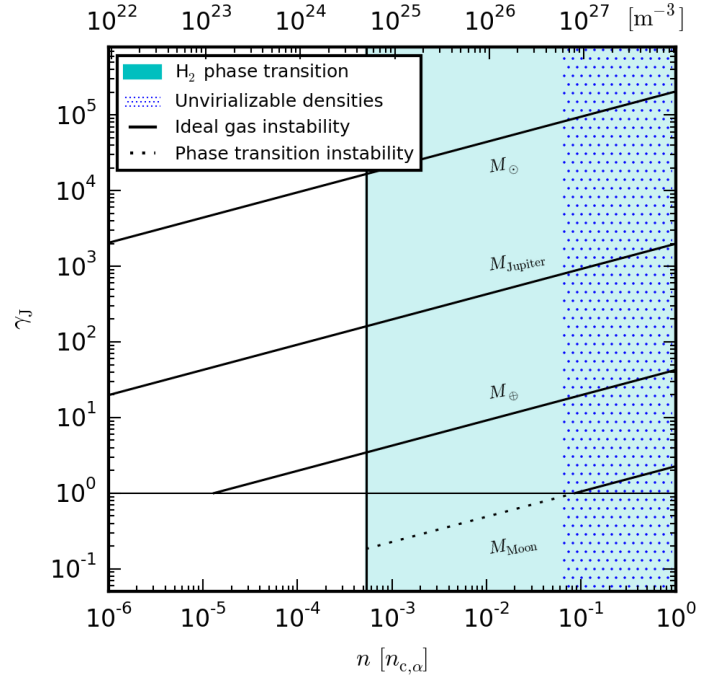


Fig. 20:  $\gamma_J$  of different total fluid masses at  $T = 10$  K, as a function of number density, indicating either ideal gas Jeans instability, or instability owing to phase transition.

etoid rises slightly as can be barely seen in Fig. 14a. Thus the question can be raised whether a small fraction of a secondary molecule (such as He in the case of molecular clouds) needs to be included in low-gravity simulations. To answer that question, simulation B75 with  $\gamma_J = 0.5$  was run again, but all  $\beta$ -molecules were removed and their mass was equally distributed to the  $\alpha$ -molecules to maintain the same gravitational potential.

Figure 19 shows the time evolution of the fraction of bound molecules of the simulations B75, B75 without  $\beta$ -molecules and B10 for comparison. Even though the two B75 simulations are similar, there are differences to be observed. The fraction of bound  $\alpha$ -molecules of the simulation B75 should correspond to the total fraction of bound molecules of the simulation without  $\beta$ -molecules, but the latter is higher; the  $\beta$ -molecules in B75 have a damping effect on the comet formation. In addition, the simulation without  $\beta$ -molecules is rising to a higher value at the end of the simulation.

The inclusion of a small fraction of a secondary molecule does change the look of the simulation by damping the comet formation of  $\alpha$ -molecules. For that reason, the inclusion of secondary molecules in more realistic simulations is useful.

#### 4.6. Physical systems

Up to now, we have looked at theoretical models, varying  $x_\alpha$  from 0 to 1, and setting the temperature and density as a fraction of the respective  $\alpha$  critical values. The critical values for  $H_2$  are  $T_c = 32.97$  K and  $n_c = 9.34 \cdot 10^{27} \text{ m}^{-3}$ . In astrophysical conditions, the He mass fraction is between  $w_{\text{He,SS}} = 0.2741$  for the solar system (Lodders 2003) and  $w_{\text{He,MW}} = 0.2486$  for the initial Big Bang mixture (Cyburt et al. 2008), which translates to number fractions  $x_{\text{He,SS}} = 0.1598$  and  $x_{\text{He,MW}} = 0.1428$ .

Figure 20 shows  $\gamma_J$  as a function of the number density for solar system abundances ( $x = 0.16$ ) and  $T = 10$  K with total masses equal to the Moon, Earth, Jupiter, and Sun.  $H_2$  is then

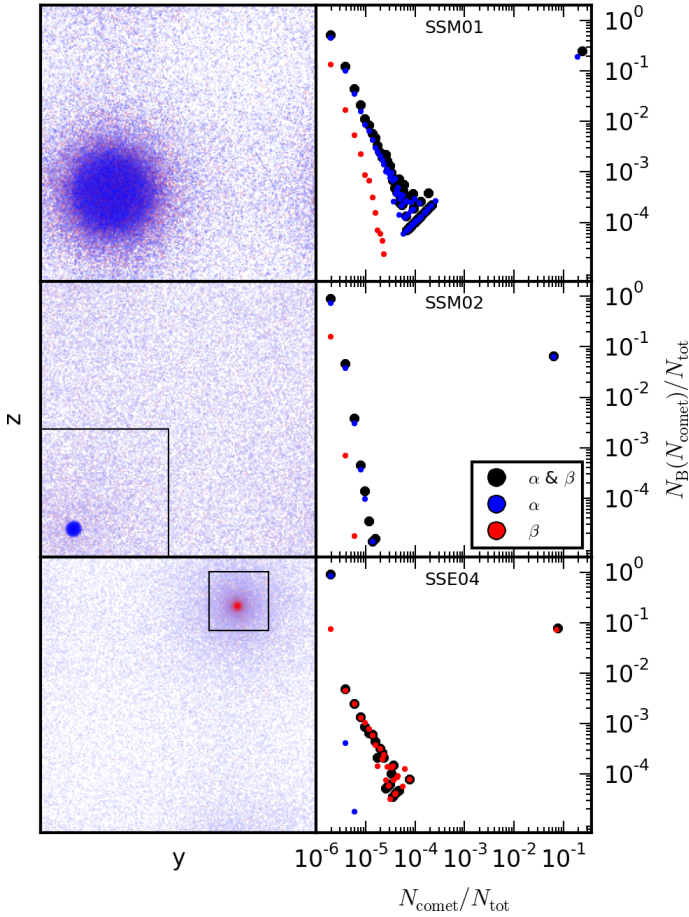


Fig. 21: Snapshots and comet-size distributions of the simulations SSM01, SSM02, and SSE04. The slice selects in depth 20% of the super-molecules. The squares in the two lower left frames are the same size as the next upper frame.

in a phase transition for  $n > 4 \cdot 10^{24} \text{ m}^{-3}$ ; only a Moon mass or below can be in a phase transition and below the Jeans criterion. The fluid is unvirializable for  $n > 6 \cdot 10^{26} \text{ m}^{-3}$ .

If we go to a lower temperature, say the CMB 2.7 K, a H<sub>2</sub> phase transition takes place for  $n > 10^{12} \text{ m}^{-3}$ . In that case, fluids with Earth mass would be chemically unstable below the ideal gas Jeans criterion for  $n \leq 3 \cdot 10^{21} \text{ m}^{-3}$  and with Jupiter mass for  $n \leq 3 \cdot 10^{16} \text{ m}^{-3}$ . Fluids with Sun mass, on the other hand, cross  $\gamma_1 = 1$  only in the gaseous phase of H<sub>2</sub>. The lowest unvirializable density  $n_- = 6 \cdot 10^{26} \text{ m}^{-3}$  does not change a lot with temperature.

The number of FFT mesh cells  $N_{\text{FFT}} \propto L^3$  and the simulation timescale  $\tau \propto L$  both directly depend on  $L \propto n^{-1/3}$ , and the total calculation duration scales as  $t_{\text{sim}} \propto \tau \cdot N_{\text{FFT}} \propto n^{-4/3}$ . For that reason, simulating a fluid at CMB temperature with densities below  $10^{20} \text{ m}^{-3}$  would translate to extremely long simulation run times with today's computers. In addition, the upper limit for the mass of super-molecules is  $m_{\text{SM,max}} \approx 5 \cdot 10^{-6} M_{\oplus}$  (see Equ. 40). Thus, the minimum number of super-molecules  $N_{\text{tot,min}} = M/m_{\text{SM,max}}$  is  $\sim 2 \cdot 10^5$ ,  $6.5 \cdot 10^7$ ,  $6.5 \cdot 10^{10}$  for simulating an Earth, Jupiter, and Sun mass, respectively. For that reason, for the time being we content ourselves to studying systems up to total mass comparable to the Earth mass.

#### 4.6.1. Planetoid formation

Three simulations were run at a temperature of  $T = 10 \text{ K}$ , which is above the critical temperature of He and below that of H<sub>2</sub>, and thus in a similar regime as the B simulations. Two simulations have a total mass equal to the Moon, with  $n \approx 10^{27} \text{ m}^{-3}$  which is above the ideal gas Jeans criterion and in the unvirializable domain, and  $n \approx 10^{26} \text{ m}^{-3}$ , which is below the Jeans criterion, and one has a total mass equal to the Earth and with  $n \approx 10^{24} \text{ m}^{-3}$ , which is above the criterion. The simulation parameters are given in Table 1.

Figure 21 shows the snapshot and comet-size distribution of the three simulations after the formation of a planetoid. The fluid of SSE04 is above the ideal gas Jeans criterion and we observe the formation a He-planetoid, surrounded by H<sub>2</sub>, similar to Sect. 4.2.1. The evolution of simulation SSM02, which is below the ideal gas Jeans criterion, leads to the formation of a rocky H<sub>2</sub> planetoid, similar to Sect. 4.2.2.

In the case of SSM01, the density lies in the unvirializable domain, resulting in a formation of many H<sub>2</sub>-grains that are heavier than the He-atoms from the very beginning. This leads to the formation of a H<sub>2</sub>-planetoid similar to Sect. 4.3.1.

## 5. Conclusions

In our first article, FP2015, we studied the gravitational instability of a fluid in a phase transition. We extrapolated the results to the ubiquitous H<sub>2</sub> and showed that the formation of cold, mostly undetectable comet- and even planet-sized rocky H<sub>2</sub> clumps is very possible. The use of only one component gives a good first impression, but in cosmic gases, there is a mass fraction of  $w \approx 25 \pm 2 \%$  He atoms.

In the present work, we studied binary fluid mixtures analytically and via numerical simulations. The results show that, depending on the circumstances, either He or H<sub>2</sub> planetoids can form.

### 5.1. Analytic results

The stability of a multicomponent fluid mixture has already been studied in the literature, mostly to study fluid binaries consisting of baryonic and dark matter. The wave number below which a fluid mixture is unstable is the sum of the Jeans wave-numbers of each component. Since the Jeans wave number is inversely proportional to  $(\partial P / \partial \rho)^{-1}$ , which is equal to zero in the case of a phase transition, a fluid mixture is unstable as soon as one of its components is in a phase transition. Physically what happens is that when one species is in a phase transition, an overdensity only increases its condensed phase fraction at constant pressure, instead of increasing pressure and producing no global force to counter gravity. The transformation from the gas to the condensed phase continues until the species is fully condensed.

We studied the evolution of unstable fluid mixtures with the widely used Lennard-Jones intermolecular potential, which reproduces the H<sub>2</sub> phase transition very well (but it reproduces the He transition, which is not essential in this work, less well). We showed, using the virial analysis of Lennard-Jones fluid mixtures, that there is a unvirializable density-domain  $\mathcal{D}$  within which the attractive forces dominate the repulsive forces for any total mass  $M$  and no virial equilibrium is possible. These states can be reached in strongly dynamical situations (e.g. during collapses) and are able to produce condensed comets particularly quickly. Dynamical friction is important to separate species and condensed comets. For instance, if H<sub>2</sub> is in a phase transition, the



formed  $H_2$  comets are heavier than the He-molecules, and precipitate in a gravitational field, producing almost pure  $H_2$  bodies.

There are three reasons to concentrate on plane-parallel initial collapses, as described in more detail in App. B:

1. In typical cosmic conditions, the fastest collapsing geometry is sheet-like, not filament- or point-like.
2. The adiabatic matter compression during collapse leads to the least heating in sheet-like geometry: in a sheet-like adiabatic collapse the gravitational energy released to the fluid is *finite* and amounts to a maximum increase of temperature by only a factor of about two, while in filament-like collapses the temperature diverges logarithmically as a function of filament radius, and in point-like collapses the temperature diverges as the inverse sphere radius.
3. Radiative cooling is the easiest in sheet-like collapse. Indeed the absorption probability in sheet-like geometry remains almost unchanged for any compression, and an initially transparent medium remains transparent, whereas the probability converges to one in filament-like and point-like geometries. Therefore, radiative cooling is barely slowed down in sheet-like collapses and, unlike in spherical or filament collapses, opacity is unable to prevent density from reaching high values. This is a crucial point for this study, as the ISM conditions are commonly thought to be far away from the  $H_2$  phase transition conditions.

## 5.2. Simulations

As in FP2015, we used super-molecules to combine the Lennard-Jones intermolecular potential together with the gravitational potential in numerical simulations. Several binary fluid mixtures were studied using two components:  $\alpha$  and  $\beta$ . Their respective properties (the most important being  $m_\alpha/m_\beta < 1$  and  $T_{c,\alpha}/T_{c,\beta} > 1$ ) were chosen to mimic a  $H_2$ -He fluid, but the general properties of the fluids were made molecule independent.

Three temperature domains can be defined: (A) above both critical temperatures, (B) between the critical temperatures, and (C) below both critical temperatures. In all three cases, the molecular fraction was varied and the fluids were simulated above and below the Jeans criterion. We used different numbers of molecules to test the scaling of the simulations. The precise number of super-molecules is not important for dynamical processes, but we found a weak dependence for segregation effects in the sense that coarser simulations exaggerate these effects.

In case (A), both components are gaseous and an introduced perturbation does not grow when the gravitational potential is below the Jeans criterion. When above the Jeans criterion, the fluid collapses and forms a gaseous planetoid. The  $\beta$ -molecules are twice as massive as the  $\alpha$ -molecules, and fall faster into the planetoid. For that reason, the planetoid consists mostly of  $\beta$ -molecules, surrounded by an  $\alpha$ -atmosphere. This is independent of the molecular fraction  $x_\alpha$ , even at very high  $x_\alpha$ -values, the planetoids consists mostly of  $\beta$ -molecules.

In case (B) and (C), the number density of the fluids was chosen so that the  $\alpha$ -component is in a phase transition for all  $x_\alpha > 0$ . In fact, both cases are very similar since in both cases the  $\beta$ -component is not in a phase transition. When the fluids are below the Jeans criterion, an instability happens because of the phase transition of the  $\alpha$ -component, which leads to the formation of  $H_2$  comets and ultimately a rocky  $\alpha$ -planetoid. This planetoid is surrounded by a  $\beta$ -atmosphere, which is getting more important with increasing gravitational potential. As in case (A), the molecular fraction  $x_\alpha$  does not matter, even at very low

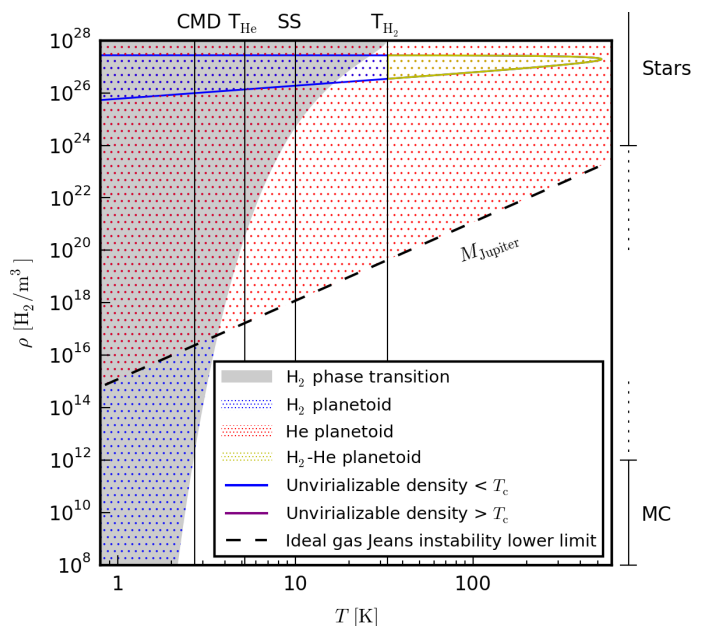


Fig. 22: Gravitational instabilities at different temperatures and densities for a fluid with Jupiter mass.

$x_\alpha$ -values, the planetoid still consists almost exclusively of  $\alpha$ -molecules.

A suprising observation occurs for cases (B) or (C) above the Jeans criterion. In that case, there is a race between the formation of small  $\alpha$ -grains owing to the phase transition and the exponential growth of the perturbation. The heaviest bodies are decelerated faster and fall into the forming planetoid first. When the  $\alpha$ -component is either gaseous or only forming very few and small comets, a  $\beta$ -planetoid forms. On the other hand, if the  $\alpha$ -component forms many grains that are heavier than the  $\beta$ -molecules, an  $\alpha$ -planetoid forms. We showed in the simulations that this race between  $\alpha$  and  $\beta$  is linked with the unvirializable density domain  $\mathcal{D}$ . If a fluid reaches this domain, the  $\alpha$ -component wins, otherwise the  $\beta$ -component wins.

### 5.2.1. Solar system abundances

In addition to the above-mentioned simulations, fluids with solar system abundances and Moon or Earth mass were simulated. As shown in Fig. 20, a fluid with Earth mass cannot be below the Jeans criterion and still in a phase transition, but with Moon mass, this is possible. In that case, a rocky  $H_2$  planetoid results. With a mass as low as the Moon, the fluid needs to be very dense to be above the Jeans criterion. In fact, the fluid would lie in the unvirializable density-domain  $\mathcal{D}$  and, thereby, a  $H_2$ -planetoid forms. For a fluid with Earth mass, on the other hand, even a relatively low-density fluid is still above the Jeans criterion. The result is a gaseous He planetoid with a  $H_2$  atmosphere.

### 5.3. Instability in $H_2$ -He fluid

Figure 22 shows different possible planetoid and comet formations due to gravitational instability for a fluid with Jupiter mass. A fluid is gaseous if it is below the phase transition domain and a fluid is solid or liquid if above. When the density is in the phase transition, it can rise without an increase of pressure.

There can be no formation below the Jeans criterion if the fluid is not in a phase transition. Most of the planetoids due to



an ideal gas Jeans collapse consist of gaseous He, but if the fluid is in the unvirializable domain  $\mathcal{D}$ , then a H<sub>2</sub> planetoid forms. This H<sub>2</sub> planetoid can be solid/liquid or gaseous depending on its temperature. If gaseous, He is able to percolate down, slowly transforming it into a He planetoid.

If the fluid is in a phase transition, we have to distinguish between a collapse above the ideal Jeans criterion, which leads to a gaseous He planetoid except in the unvirializable domain, where it becomes a rocky H<sub>2</sub> planetoid, and in a collapse below the ideal Jeans criterion, which also leads to a rocky H<sub>2</sub> planetoid.

The usual average density domain of molecular clouds lies between  $10^8$  and  $10^{12}$  H<sub>2</sub>/m<sup>3</sup> and, with such a density, a H<sub>2</sub> phase transition is only possible at temperatures below  $\sim 5$  K. However, molecular clouds are observed to follow a fractal mass distribution over a minimum of 4–6 orders of magnitude in column densities, so the average density is not a quantity to characterize molecular clouds properly. Since we know that stars form with densities  $\sim 10^{29}$  H<sub>2</sub>/m<sup>3</sup>, by continuing this argument, intermediate states covering all this density interval have to exist.

Fluids with a high total mass, especially with stellar mass or above, reach the ideal gas Jeans criterion very quickly leading to gaseous He-planetoids. Fluids with lower total mass, however, as for example the cold globules observed in the Helix nebula, especially with Earth mass and below, have the ideal gas Jeans criterion at much higher densities and are in the phase transition domain before being above the ideal gas Jeans criterion.

#### 5.4. Perspectives

This and the previous FP2015 study show that the cold ISM physics is much richer than previously imagined. The formation of substellar gaseous or rocky condensed bodies by the H<sub>2</sub> phase transition combined to gravity, appears natural once we recognize that collapses proceed most of the time along the sequence pancake, filament, and point, and in the first sheet-like phase high densities allowing a H<sub>2</sub> phase transition can be reached if the initial medium temperature is below  $\sim 15$  K. This temperature limit would be even higher if radiative cooling had been considered. In the isothermal case this limit is  $\sim 33$  K.

Most of the ISM cold gas must therefore pass over molecular cloud lifetimes ( $\sim 10^6 - 10^8$  yr) through such brief ( $\sim 10^2 - 10^4$  yr) singular sheet-like collapses where density diverges but not temperature. Observationally, such events are difficult to detect because of the limited increase of temperature, opacity, and column density all along the collapse, while reaching high volume densities. When seen edge-on such sheet-like collapses would look like filaments.

The simulations we were able to perform are still very limited in total mass. Including He is necessary but this provides a number of complications with respect to the pure H<sub>2</sub> case, and widens the general picture found in FP2015. Combining the accumulated experience of large-scale gas phase simulations by other authors (e.g. Renaud et al. 2013; Butler et al. 2015), we can easily extrapolate what larger simulations should produce with micro-AU resolution. Instead of one planetoid per simulation box, pc-sized sheet-like collapses should show filaments with longer lifetimes, which would funnel H<sub>2</sub> condensed bodies and produce a spectrum of planetoids, comets, and occasionally stars. The leftover condensed cold substellar bodies should then start to evaporate according to the ambient radiation flux and depth of their gravitational potential. The lifetime of such bodies should be short near the centre of galaxies, but much longer at the periphery of galaxies, or even in intergalactic space, especially in cosmic filaments. One can postulate that, especially

at the periphery of disk galaxies where the radiation heating is low, some fraction of the dark baryons can be trapped in the form of such condensed bodies. We plan to pursue further simulation work to deepen our understanding of the processes associating phase transition with gravitational dynamics.

*Acknowledgements.* This work is supported by the STARFORM Sinergia Project funded by the Swiss National Science Foundation. We thank the LAMMPS team for providing a powerful open source tool to the scientific community.

## References

- Air Liquide. 1976, Gas Encyclopedia (Editor Elsevier)
- Banaszak, M., Chiew, Y. C., & Radosz, M. 1995, *Fluid Phase Equilibria*, 111, 161
- Becker, A., Lorenzen, W., Fortney, J. J., et al. 2014, *The Astrophysical Journal Supplement Series*, 215, 21
- Berthelot, D. 1898, *Comptes rendus hebdomadaires des séances de l'Académie des Sciences*
- Bolatto, A. D., Wolfire, M., & Leroy, A. K. 2013, *Annual Review of Astronomy and Astrophysics*, 51, 207
- Butler, M. J., Tan, J. C., & Van Loo, S. 2015, *The Astrophysical Journal*, 805, 1
- Caillol, J. M. 1998, *Journal of Chemical Physics*, 109, 4885
- Chandrasekhar, S. 1943, *The Astrophysical Journal*, 97, 255
- Chen, J., Mi, J.-G., & Chan, K.-Y. 2001, *Fluid Phase Equilibria*, 178, 87
- Clerk-Maxwell, J. 1875, *Nature*, 11, 357
- Cybur, R. H., Fields, B. D., & Olive, K. A. 2008, *Journal of Cosmology and Astro-Particle Physics*, 11, 012
- de Carvalho, J. P. M. & Macedo, P. G. 1995, *Astronomy and Astrophysics*, 299, 326
- Draine, B. T. 2011, *Physics of the Interstellar and Intergalactic Medium*
- Elmegreen, B. G. & Scalo, J. 2004, *Annual Review of Astronomy and Astrophysics*, 42, 211
- Füglistaler, A. & Pfenniger, D. 2015, *Astronomy & Astrophysics*, 578, A18, arXiv: 1503.04788
- Grishchuk, L. P. & Zeldovich, Y. B. 1981, *Soviet Astronomy*, 25, 267
- Jeans, J. H. 1902, *Royal Society of London Philosophical Transactions Series A*, 199, 1
- Jog, C. J. & Solomon, P. M. 1984a, *The Astrophysical Journal*, 276, 127
- Jog, C. J. & Solomon, P. M. 1984b, *The Astrophysical Journal*, 276, 114
- Johnston, D. C. 2014, *ArXiv e-prints*, 1402, 1205
- Koci, L., Ahuja, R., Belonoshko, A. B., & Johansson, B. 2007, *Journal of Physics Condensed Matter*, 19, 016206
- Landau, L. D. & Lifshitz, E. M. 1975, *The classical theory of fields*
- Lin, C. C., Mestel, L., & Shu, F. H. 1965, *The Astrophysical Journal*, 142, 1431
- Lodders, K. 2003, *The Astrophysical Journal*, 591, 1220
- Lorentz, H. A. 1881, *Annalen der Physik*, 248, 127
- Padmanabhan, T. 1990, *Physics Reports*, 188, 285
- Pfenniger, D. & Combes, F. 1994, *Astronomy and Astrophysics*, 285, 94
- Pfenniger, D., Combes, F., & Martinet, L. 1994, *Astronomy and Astrophysics*, 285, 79
- Plimpton, S. 1995, *Journal of Computational Physics*, 117, 1
- Renaud, F., Bournaud, F., Emsellem, E., et al. 2013, *Monthly Notices of the Royal Astronomical Society*, 436, 1836
- Safa, Y. & Pfenniger, D. 2008, *European Physical Journal B*, 66, 337
- Saumon, D., Chabrier, G., & van Horn, H. M. 1995, *The Astrophysical Journal Supplement Series*, 99, 713
- Shandarin, S. F., Melott, A. L., McDavitt, K., Pauls, J. L., & Tinker, J. 1995, *Physical Review Letters*, 75, 7
- Streett, W. B. 1973, *The Astrophysical Journal*, 186, 1107
- van der Waals, J. D. 1910, *Koninklijke Nederlandse Akademie van Wetenschappen Proceedings Series B Physical Sciences*, 13, 1253
- Volkov, E. & Ortega, V. G. 2000, *Monthly Notices of the Royal Astronomical Society*, 313, 112
- Vorberger, J., Tamblyn, I., Militzer, B., & Bonev, S. A. 2007, *Physical Review B*, 75, 024206
- Zel'dovich, Y. B. 1970, *Astronomy and Astrophysics*, 5, 84

## Appendix A: Jeans instability

We first recall the classical Jeans criterion for a one-component fluid, and then we show how the same approach can be used to find the solution of a two-component fluid. See Grishchuk & Zeldovich (1981) for the solution of an  $n$ -component fluid.

### Appendix A.1: One component

The equations for conservation of mass and momentum and for the gravitational potential of a fluid are written as

$$\frac{\partial \rho}{\partial t} + \nabla \cdot (\rho \mathbf{v}) = 0, \quad (\text{A.1})$$

$$\frac{\partial \rho \mathbf{v}}{\partial t} + \nabla \cdot (\rho \mathbf{v} \mathbf{v}) + \nabla P + \rho \nabla \Phi = 0, \quad (\text{A.2})$$

$$\nabla \cdot \nabla \Phi - 4\pi G \rho = 0. \quad (\text{A.3})$$

Following Jeans (1902), we supersede these equations with perturbation terms in the  $x$  direction  $\rho = \rho_0 + \delta\rho$ ,  $P = P_0 + \delta P$ ,  $\Phi = \Phi_0 + \delta\Phi$  and  $\mathbf{v} = \mathbf{v}_0 + \delta\mathbf{v}$  with  $\delta\mathbf{v} = (\delta v, 0, 0)^T$ , linearizing the equations and setting  $\delta P = \left(\frac{\partial P}{\partial \rho}\right)_s \delta\rho$ , i.e.

$$\frac{\partial \delta\rho}{\partial t} + \rho_0 \nabla \cdot \delta\mathbf{v} = 0, \quad (\text{A.4})$$

$$\rho_0 \frac{\partial \delta v}{\partial t} + \left(\frac{\partial P}{\partial \rho}\right)_s \nabla \delta\rho + \rho_0 \nabla \delta\Phi = 0, \quad (\text{A.5})$$

$$\nabla \cdot \nabla \delta\Phi - 4\pi G \delta\rho = 0. \quad (\text{A.6})$$

This system of partial differential equations is transformed to an algebraic system of linear equations in the Fourier space:  $\delta A = \int dk \hat{A}(k) \exp[i(kx - \omega t)]$ , where  $A$  represents  $\rho$ ,  $v$ , and  $\Phi$ . The passage to Fourier space transforms the differential operators  $\partial/\partial t$  and  $\partial/\partial x$  to multiplications by  $-i\omega$  and  $ik$ , respectively,

$$-i\omega \hat{\rho} + ik \rho_0 \hat{v} = 0, \quad (\text{A.7})$$

$$-i\omega \rho_0 \hat{v} + ik \left(\frac{\partial P}{\partial \rho}\right)_s \hat{\rho} + ik \rho_0 \hat{\Phi} = 0, \quad (\text{A.8})$$

$$-k^2 \hat{\Phi} - 4\pi G \hat{\rho} = 0, \quad (\text{A.9})$$

which can be written in matrix form  $\mathbf{A} \cdot \mathbf{x} = \mathbf{0}$ ,

$$\begin{bmatrix} \omega & k\rho_0 & 0 \\ k(\partial P/\partial \rho)_s & \omega\rho_0 & k\rho_0 \\ -4\pi G & 0 & -k^2 \end{bmatrix} \cdot \begin{bmatrix} \hat{\rho} \\ \hat{v} \\ \hat{\Phi} \end{bmatrix} = \begin{bmatrix} 0 \\ 0 \\ 0 \end{bmatrix}. \quad (\text{A.10})$$

Non-trivial solutions for  $\mathbf{x}$  require that the determinant of  $\mathbf{A}$  vanishes,

$$\det(\mathbf{A}) = k^2 \rho_0 \left[ \omega^2 + 4\pi G \rho_0 - k^2 \left(\frac{\partial P}{\partial \rho}\right)_s \right], \quad (\text{A.11})$$

which is the case for either  $k = 0$ , or

$$\omega^2 = k^2 \left(\frac{\partial P}{\partial \rho}\right)_s - 4\pi G \rho_0. \quad (\text{A.12})$$

A fluid is unstable if  $\omega^2 < 0$ , which is the case if

$$k^2 < k_J^2 \equiv \frac{4\pi G \rho_0}{(\partial P/\partial \rho)_s}. \quad (\text{A.13})$$

### Appendix A.2: Two components

Having two components  $\alpha$  and  $\beta$ , the mass and momentum conservation have to be fulfilled for each component as follows:

$$\frac{\partial \rho_\alpha}{\partial t} + \nabla \cdot (\rho_\alpha \mathbf{v}_\alpha) = 0, \quad (\text{A.14})$$

$$\frac{\partial \rho_\beta}{\partial t} + \nabla \cdot (\rho_\beta \mathbf{v}_\beta) = 0, \quad (\text{A.15})$$

$$\frac{\partial \rho_\alpha \mathbf{v}_\alpha}{\partial t} + \nabla \cdot (\rho_\alpha \mathbf{v}_\alpha \mathbf{v}_\alpha) + \nabla P_\alpha + \rho_\alpha \nabla \Phi = 0, \quad (\text{A.16})$$

$$\frac{\partial \rho_\beta \mathbf{v}_\beta}{\partial t} + \nabla \cdot (\rho_\beta \mathbf{v}_\beta \mathbf{v}_\beta) + \nabla P_\beta + \rho_\beta \nabla \Phi = 0, \quad (\text{A.17})$$

$$\nabla \cdot \nabla \Phi - 4\pi G (\rho_\alpha + \rho_\beta) = 0. \quad (\text{A.18})$$

Superseding, as in App. A.1, these equations with perturbation terms  $A_\alpha = A_{\alpha 0} + \delta A_\alpha$  and  $A_\beta = A_{\beta 0} + \delta A_\beta$  in the  $x$  direction and linearizing them yields

$$\frac{\partial \delta \rho_\alpha}{\partial t} + \rho_\alpha \nabla \cdot \delta \mathbf{v}_\alpha = 0, \quad (\text{A.19})$$

$$\frac{\partial \delta \rho_\beta}{\partial t} + \rho_\beta \nabla \cdot \delta \mathbf{v}_\beta = 0, \quad (\text{A.20})$$

$$\rho_\alpha \frac{\partial \delta v_\alpha}{\partial t} + \left(\frac{\partial P_\alpha}{\partial \rho_\alpha}\right)_s \nabla \delta \rho_\alpha + \rho_\alpha \nabla \delta \Phi = 0, \quad (\text{A.21})$$

$$\rho_\beta \frac{\partial \delta v_\beta}{\partial t} + \left(\frac{\partial P_\beta}{\partial \rho_\beta}\right)_s \nabla \delta \rho_\beta + \rho_\beta \nabla \delta \Phi = 0, \quad (\text{A.22})$$

$$\nabla \cdot \nabla \delta \Phi - 4\pi G (\delta \rho_\alpha + \delta \rho_\beta) = 0, \quad (\text{A.23})$$

which transform into a linear equation system in Fourier space,

$$-i\omega \hat{\rho}_\alpha + ik \rho_{\alpha 0} \hat{v}_\alpha = 0, \quad (\text{A.24})$$

$$-i\omega \hat{\rho}_\beta + ik \rho_{\beta 0} \hat{v}_\beta = 0, \quad (\text{A.25})$$

$$-i\omega \rho_{\alpha 0} \hat{v}_\alpha + ik \left(\frac{\partial P_\alpha}{\partial \rho_\alpha}\right)_s \hat{\rho}_\alpha + ik \rho_{\alpha 0} \hat{\Phi} = 0, \quad (\text{A.26})$$

$$-i\omega \rho_{\beta 0} \hat{v}_\beta + ik \left(\frac{\partial P_\beta}{\partial \rho_\beta}\right)_s \hat{\rho}_\beta + ik \rho_{\beta 0} \hat{\Phi} = 0, \quad (\text{A.27})$$

$$-k^2 \hat{\Phi} - 4\pi G (\hat{\rho}_\alpha + \hat{\rho}_\beta) = 0. \quad (\text{A.28})$$

This can be written in the matrix form  $\mathbf{A} \cdot \mathbf{x} = \mathbf{0}$ , defining  $c_\alpha^2 = (\partial P_\alpha / \partial \rho_\alpha)_s$  and  $c_\beta^2 = (\partial P_\beta / \partial \rho_\beta)_s$  as follows:

$$\begin{bmatrix} \omega & 0 & k\rho_{\alpha 0} & 0 & 0 \\ 0 & \omega & 0 & k\rho_{\beta 0} & 0 \\ k c_\alpha^2 & 0 & \omega \rho_{\alpha 0} & 0 & k \rho_{\alpha 0} \\ 0 & k c_\beta^2 & 0 & \omega \rho_{\beta 0} & k \rho_{\beta 0} \\ -4\pi G & -4\pi G & 0 & 0 & -k^2 \end{bmatrix} \cdot \begin{bmatrix} \hat{\rho}_\alpha \\ \hat{\rho}_\beta \\ \hat{v}_\alpha \\ \hat{v}_\beta \\ \hat{\Phi} \end{bmatrix} = \begin{bmatrix} 0 \\ 0 \\ 0 \\ 0 \\ 0 \end{bmatrix}. \quad (\text{A.29})$$

In order to simplify, we set  $\Gamma_\alpha = 4\pi G \rho_{\alpha 0}$  and  $\Gamma_\beta = 4\pi G \rho_{\beta 0}$  and find the following determinant:

$$\det(\mathbf{A}) = k^2 \rho_{\alpha 0} \rho_{\beta 0} \left[ \omega^4 + (\Gamma_\alpha + \Gamma_\beta - k^2(c_\alpha^2 + c_\beta^2)) \omega^2 + k^2 (-\Gamma_\beta c_\alpha^2 - \Gamma_\alpha c_\beta^2 + k^2 c_\alpha^2 c_\beta^2) \right]. \quad (\text{A.30})$$

Again, to have a non-trivial solution, its determinant must be zero, which, in the case of  $k \neq 0$ , is

$$\omega^4 + (\Gamma_\alpha + \Gamma_\beta - k^2(c_\alpha^2 + c_\beta^2)) \omega^2 - k^2 (\Gamma_\beta c_\alpha^2 + \Gamma_\alpha c_\beta^2 - k^2 c_\alpha^2 c_\beta^2) = 0, \quad (\text{A.31})$$

with the following solution for  $\omega^2$ :

$$(\omega^2)_{1,2} = -\frac{1}{2}(\Gamma_\alpha + \Gamma_\beta - k^2(c_\alpha^2 + c_\beta^2)) \pm \sqrt{\frac{1}{4}(\Gamma_\alpha + \Gamma_\beta - k^2(c_\alpha^2 + c_\beta^2))^2 + k^2(\Gamma_\beta c_\alpha^2 + \Gamma_\alpha c_\beta^2 - k^2 c_\alpha^2 c_\beta^2)}. \quad (\text{A.32})$$

Setting  $\omega^2 = 0$  in Equ. (A.31) yields

$$k^2(-\Gamma_\beta c_\alpha^2 - \Gamma_\alpha c_\beta^2 + k^2 c_\alpha^2 c_\beta^2) = 0, \quad (\text{A.33})$$

with the following solution:

$$k_{\text{GZ}}^2 \equiv \frac{\Gamma_\alpha}{c_\alpha^2} + \frac{\Gamma_\beta}{c_\beta^2}, \quad (\text{A.34})$$

a fluid is unstable for  $\omega^2 < 0$  or  $\omega^2 \in \mathfrak{I}$ , which is the case for  $k^2 < k_{\text{GZ}}^2$ .

### Appendix A.2.1: Phase transition

In the case of a phase transition, one of the pressure derivatives is equal to zero. Setting  $c_\alpha = 0$  in Equ. (A.31) we get

$$\omega^4 + [\Gamma_\alpha + \Gamma_\beta - k^2 c_\beta^2] \omega^2 - \Gamma_\alpha k^2 c_\beta^2 = 0, \quad (\text{A.35})$$

and its solutions is written as

$$\omega^2 = -\frac{1}{2}(\Gamma_\alpha + \Gamma_\beta - k^2 c_\beta^2) \pm \sqrt{\frac{1}{4}(\Gamma_\alpha + \Gamma_\beta - k^2 c_\beta^2)^2 + \Gamma_\alpha k^2 c_\beta^2}. \quad (\text{A.36})$$

Setting  $\omega^2 = 0$  in Equ. (A.35), only the trivial  $k = 0$  is a solution. Since

$$(\Gamma_\alpha + \Gamma_\beta - k^2 c_\beta^2)^2 < (\Gamma_\alpha + \Gamma_\beta - k^2 c_\beta^2)^2 + 4\Gamma_\alpha k^2 c_\beta^2, \quad (\text{A.37})$$

the upper sign solution of Equ. (A.36) is always positive and the lower sign solution is always negative for any  $k$ . Therefore one  $\omega$ -solution of Equ. (A.36) is always negative and thus unstable, independent of the strength of either  $\Gamma_\alpha$  or  $\Gamma_\beta$ .

## Appendix B: Energy and radiation transfer during the contraction of a sphere towards an ellipsoid

We consider a non-rotating sphere of radius  $r$  initially in unstable equilibrium, which contracts at constant mass as an ellipsoid with semi-principal axes  $a$ ,  $b$ , and  $c$  (see Fig. B.1). In a sheet-like collapse, two semi-axes remain the same ( $a = b = r$ ) while one is decreasing ( $c = \varepsilon r$ ), leading to an oblate spheroid. In a filament-like collapse, one semi-axis remains the same ( $a = r$ ), while two are decreasing together ( $b = c = \varepsilon r$ ), leading to a prolate spheroid. In a point-like collapse, all the three semi-axes decrease together ( $a = b = c = \varepsilon r$ ), remaining a sphere. During compression, density increases by a factor  $Z = n/n_0$ . Since the ellipsoid volume is  $V_{\text{ell}} = 4/3 \pi abc$ , compression changes as:  $\varepsilon_{\text{oblate}} = Z^{-1}$ ,  $\varepsilon_{\text{prolate}} = Z^{-1/2}$ , and  $\varepsilon_{\text{sphere}} = Z^{-1/3}$ .

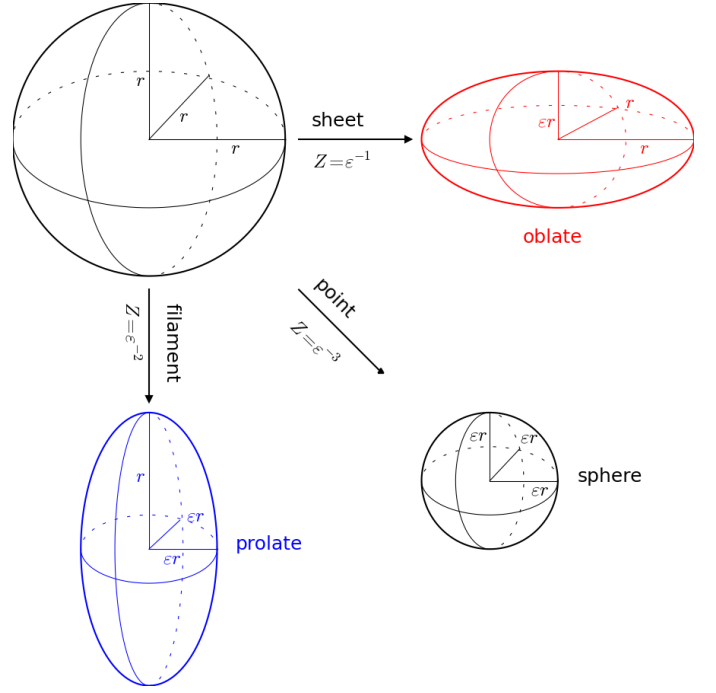


Fig. B.1: Collapsing geometries.

### Appendix B.1: Gravitational energy

The gravitational energy difference between the initial sphere and subsequent ellipsoids must be released as additional thermal energy. The gravitational energy of a revolution ellipsoid, with  $E_{G,0} = E_{G,\text{sphere}}(r) = -(3/5)GM^2/r$  (Landau & Lifshitz 1975), is written as

$$\frac{E_{\text{oblate}}(Z)}{E_{G,0}} = \frac{\arccos(Z^{-1})}{\sqrt{1-Z^{-2}}} = \frac{\pi}{2} - Z^{-1} + O(Z^{-2}), \quad (\text{B.1})$$

$$\frac{E_{\text{prolate}}(Z)}{E_{G,0}} = \frac{\text{arccosh}(\sqrt{Z})}{\sqrt{1-Z^{-1}}} = \log(2\sqrt{Z}) + O\left(\frac{\log(Z)}{Z}\right), \quad (\text{B.2})$$

$$\frac{E_{\text{sphere}}(Z)}{E_{G,0}} = Z^{1/3}. \quad (\text{B.3})$$

Sheet-like contraction leads to infinite densities with *finite* temperature increase, which is much more favourable for reaching condensation conditions that filament-like or point-like contractions.

We show now that the maximum relative temperature increase of an initial perfect gas sphere initially in equilibrium is bounded. State 0 is the initial (unstable) equilibrium sphere case, and state 1 is any later, denser case that is not necessarily in equilibrium. Since in equilibrium, the initial state respects the virial condition,

$$E_{G,0} + 2E_{\text{kin},0} = 0, \quad (\text{B.4})$$

where  $E_{\text{kin},0}$  is the kinetic energy. Since at rest, the initial sphere kinetic energy consists only of microscopic motion, and is proportional to the initial temperature  $T_0$ .

The initial and later total energies are,

$$E_{\text{tot},0} = E_{G,0} + E_{\text{kin},0}, \quad (\text{B.5})$$

$$E_{\text{tot},1} = E_{G,1} + E_{\text{kin},1}. \quad (\text{B.6})$$

Taking into account possible radiative cooling, we suppose  $E_{\text{tot},1} \leq E_{\text{tot},0}$ , which leads to, using the initial virial condition,

$$\frac{T_1}{T_0} \leq \frac{E_{\text{kin},1}}{E_{\text{kin},0}} \leq 2 \frac{E_{G,1}}{E_{G,0}} - 1. \quad (\text{B.7})$$

The first inequality takes into account that state 1 is not necessarily in equilibrium; some kinetic energy may be attributed to macroscopic motion.

Thus, using the above potential energy ratios, in the case of an oblate spheroid contraction,

$$\frac{T_1}{T_0} \leq \pi - 1 - 2Z^{-1} + O(Z^{-2}), \quad (\text{B.8})$$

that is, the final temperature cannot exceed  $\pi - 1 \approx 2.1$  times the initial temperature. In the case of a prolate spheroid contraction, temperature is logarithmically bounded as  $Z$  increases,

$$\frac{T_1}{T_0} \leq \log(4Z) - 1 + O\left(\frac{\log(Z)}{Z}\right), \quad (\text{B.9})$$

while in a spherical contraction, temperature is bounded by the cubic root of compression,

$$\frac{T_1}{T_0} \leq 2Z^{1/3} - 1. \quad (\text{B.10})$$

### Appendix B.2: Radiative cooling

Energy lost by radiation lowers temperature, but if opacity increases during contraction at some point the radiative cooling rate drops below the heating rate as a result of gravitational energy conversion, thereby slowing down the collapse. Here we show with simple arguments how opacity changes when continuously contracting an initial sphere towards denser, smaller spheres, or towards denser revolution of oblate or prolate kinds of ellipsoids, keeping the longest axes constant and assuming uniform densities at any stage and constant absorption cross sections.

#### Appendix B.2.1: Optical depth

The optical depth  $\tau$  in the cumulated absorption over a photon path  $\ell$ :  $\tau \equiv \int_0^\ell \sigma n d\ell$ , where  $\sigma$  is the absorption cross section of individual atoms with number density  $n$ . The central optical depth, calculated from the centre to the ellipsoid edge along some direction, is a first order estimator of the average optical depth. We compare the optical depth  $\tau_0 = r\sigma n_0$  for the initial sphere with the later spheres. For revolution ellipsoids, where  $a$  and  $c$  are the semi-long and short axes, respectively, the distance from the centre to some point on the edge is  $\ell(\theta) = ac / \sqrt{a^2 \sin^2 \theta + c^2 \cos^2 \theta}$  for oblate spheroids and  $\ell(\theta) = ac / \sqrt{a^2 \cos^2 \theta + c^2 \sin^2 \theta}$  for prolate spheroids. The angle  $\theta$  vanishes at the spheroid equator. Since the ellipticity  $\varepsilon = c/a$  varies as  $Z^{-1}$ ,  $Z^{-1/2}$ , and  $Z^{-1/3}$  in the oblate, prolate, and spherical cases, respectively, the optical depth ratios as functions of compression  $Z$  and  $\theta$  are found to be

$$\frac{\tau_{\text{oblate}}}{\tau_0} = \frac{1}{\sqrt{\sin^2 \theta + Z^{-2} \cos^2 \theta}}, \quad (\text{B.11})$$

$$\frac{\tau_{\text{prolate}}}{\tau_0} = \frac{Z^{1/2}}{\sqrt{\cos^2 \theta + Z^{-1} \sin^2 \theta}}, \quad (\text{B.12})$$

$$\frac{\tau_{\text{sphere}}}{\tau_0} = Z^{2/3}. \quad (\text{B.13})$$

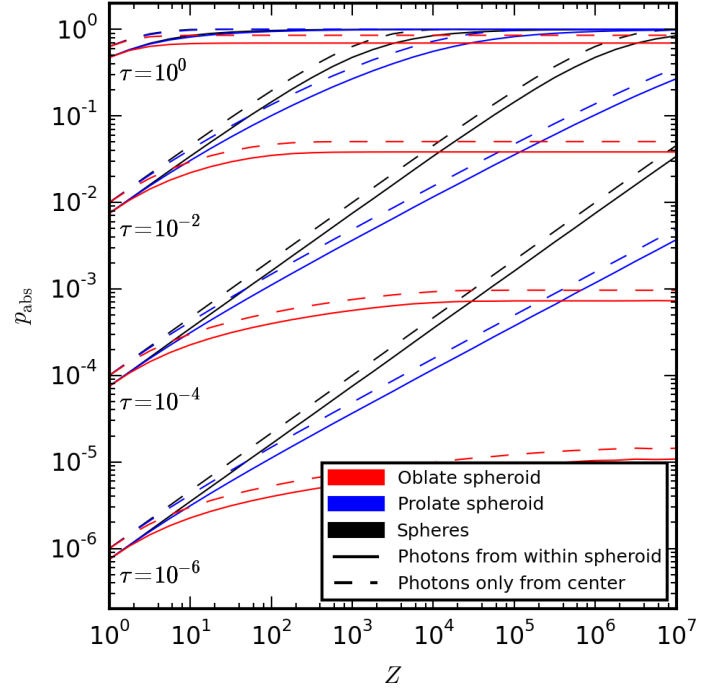


Fig. B.2: Absorption probability in contracting spheroids as function of compression  $Z > 1$  calculated by Monte Carlo simulation. At  $Z = 1$  all cases are spherical. The photons start either at the centre only or anywhere inside the ellipsoid in random directions. Different cases are represented where the initial sphere optical depth  $\tau_0$  is indicated.

Thus, in the oblate case the central optical depth ratio does not change along the poles and at high compression remains barely increased over most directions. In the prolate case it increases least along the equator, but is proportional to the square root of compression. In the spherical case it increases most rapidly as a power  $2/3$  of compression. Thus sheet-like compression provides the least optical depth increase and spherical compression the most.

#### Appendix B.2.2: Global absorption

One can refine the previous estimate for cooling by calculating, for any point inside an ellipsoid, the probability for a photon to be absorbed. For a given optical depth  $\tau$  the absorption probability is  $p = 1 - \exp(-\tau)$ . The global probability of absorption must be calculated for all solid angles for all points. These 4- or 5-dimensional integrals for bi- or tri-axial ellipsoids does not seem to be solvable analytically, and straightforward numerical quadratures would be expensive. Thus we resort to a Monte Carlo draw to estimate these quantities. We pick randomly and uniformly a number of points inside the ellipsoid and a random, uniform directional unit vector  $\mathbf{n}$ , and find the two distances  $\ell_1$ ,  $\ell_2$ , to the edge of the ellipsoid, allowing us to calculate two optical depths  $\tau_1$ ,  $\tau_2$ , and the corresponding absorption probabilities  $p_1$ ,  $p_2$  for each point. Knowing the starting position  $\mathbf{x}$  inside the ellipsoid ( $a, b, c$ ) and the direction vector  $\mathbf{n}$ , we find the two signed distances to the ellipsoid edge by solving the quadratic equation  $(x + \ell n_x)/a^2 + (y + \ell n_y)^2/b^2 + (z + \ell n_z)^2/c^2 = 1$  for  $\ell$ . Explicitly, noting  $\alpha = a^{-2}$ ,  $\beta = b^{-2}$ ,  $\gamma = c^{-2}$ , for each point

$\mathbf{x} = [x, y, z]$  the procedure becomes

$$A = \alpha n_x^2 + \beta n_y^2 + \gamma n_z^2, \quad (\text{B.14})$$

$$B = \alpha x n_x + \beta y n_y + \gamma z n_z, \quad (\text{B.15})$$

$$C = \alpha x^2 + \beta y^2 + \gamma z^2 - 1, \quad (\text{B.16})$$

$$D = \sqrt{B^2 - AC}, \quad (\text{B.17})$$

$$\ell_1 = -(D + B)/A, \quad \ell_2 = (D - B)/A. \quad (\text{B.18})$$

For each set of  $\ell_i$ , average absorption probabilities can be found for a range of  $\sigma$ s. The two absorption probabilities  $p_i = 1 - \exp(-\sigma n |\ell_i|)$ ,  $i = 1, 2$ , provide two distinct probabilities for each point. Each set of  $p_i$ s should converge towards a similar average value. The difference allows us to check the error obtained with a finite number of points. Between  $2 \cdot 10^4$  (sphere case) and  $3 \cdot 10^7$  points (oblate spheroid case) were drawn such that the  $\log_{10} p_i$  between the two sets differ by at most 0.01. The result is shown in Fig. B.2. The error bars are comparable or smaller than the thickness of the curve.

The sphere and prolate spheroid cases quickly become optically thick, increasing as  $Z^{2/3}$  and  $Z^{1/2}$ , respectively, in the optically thin regime. In contrast, the absorption of a contracting optically thin oblate spheroid increases logarithmically until it reaches  $Z\tau_0 \sim 1$  beyond which it remains approximately constant; in other words if the initial state is optically thin, it remains so even after infinite compression. The emission signature of a collapsing sheet should therefore remain observationally barely noticeable, since both temperature and optical thickness increase by very modest factors in comparison with the other geometries.

Fig. 2 shows how an initial sphere at  $T = 10$  K,  $P = 10^{-12}$  Pa would change its temperature and pressure when contracting adiabatically, changing its gravitational energy into thermal energy. Clearly the sheet-like collapse is the most favourable geometry for reaching the H<sub>2</sub> phase transition regime. Including radiative cooling, which is the fastest in sheet-like geometry, can only help in this regard.



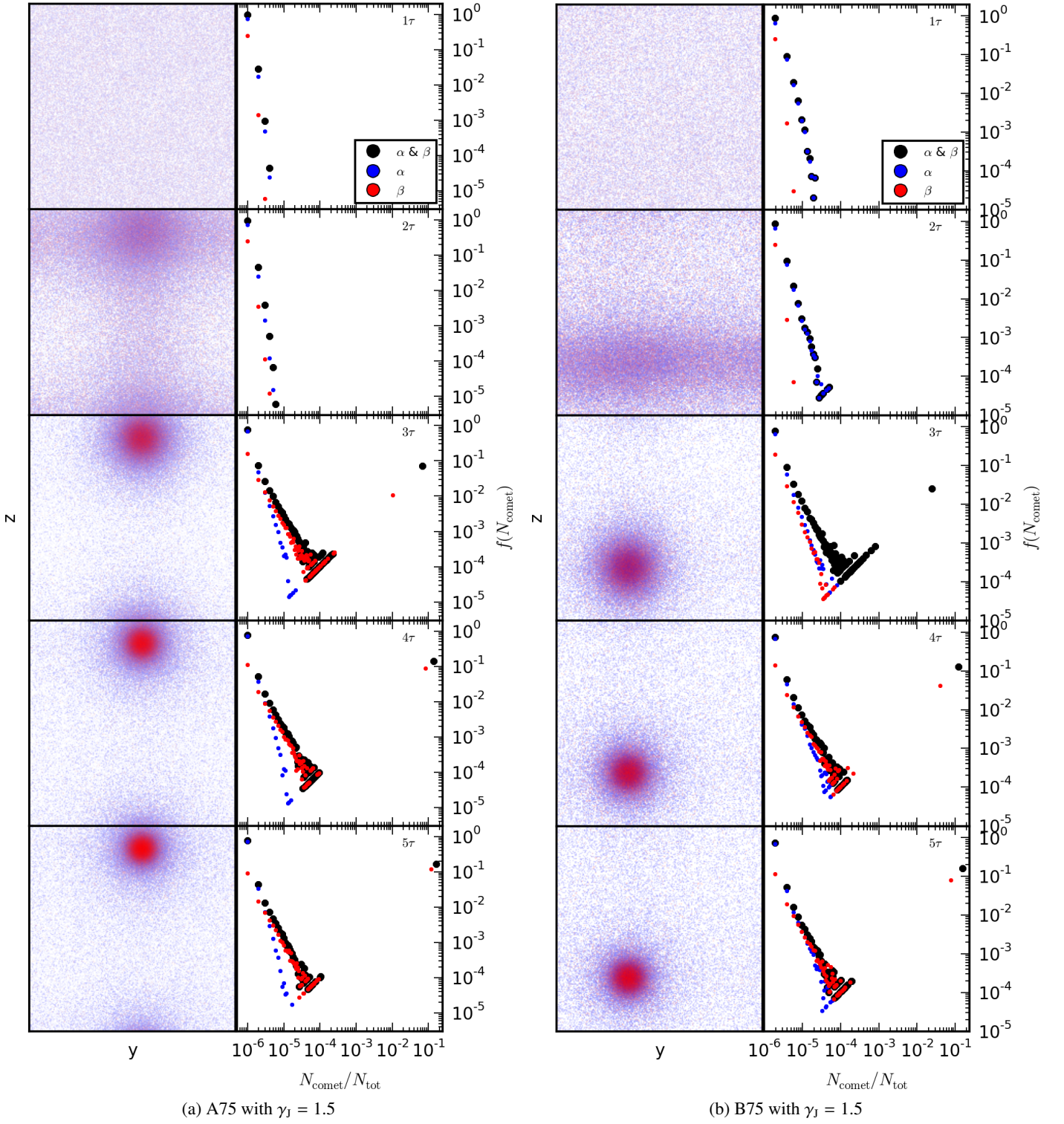


Fig. 10: Time sequence of the simulations A75 and B75. On the left side, the slice shows in depth 20% of the super-molecules. On the right side,  $N_{\text{comet}}$  is the number of super-molecules in one comet and  $f(N_B)$  is the comet size distribution function.

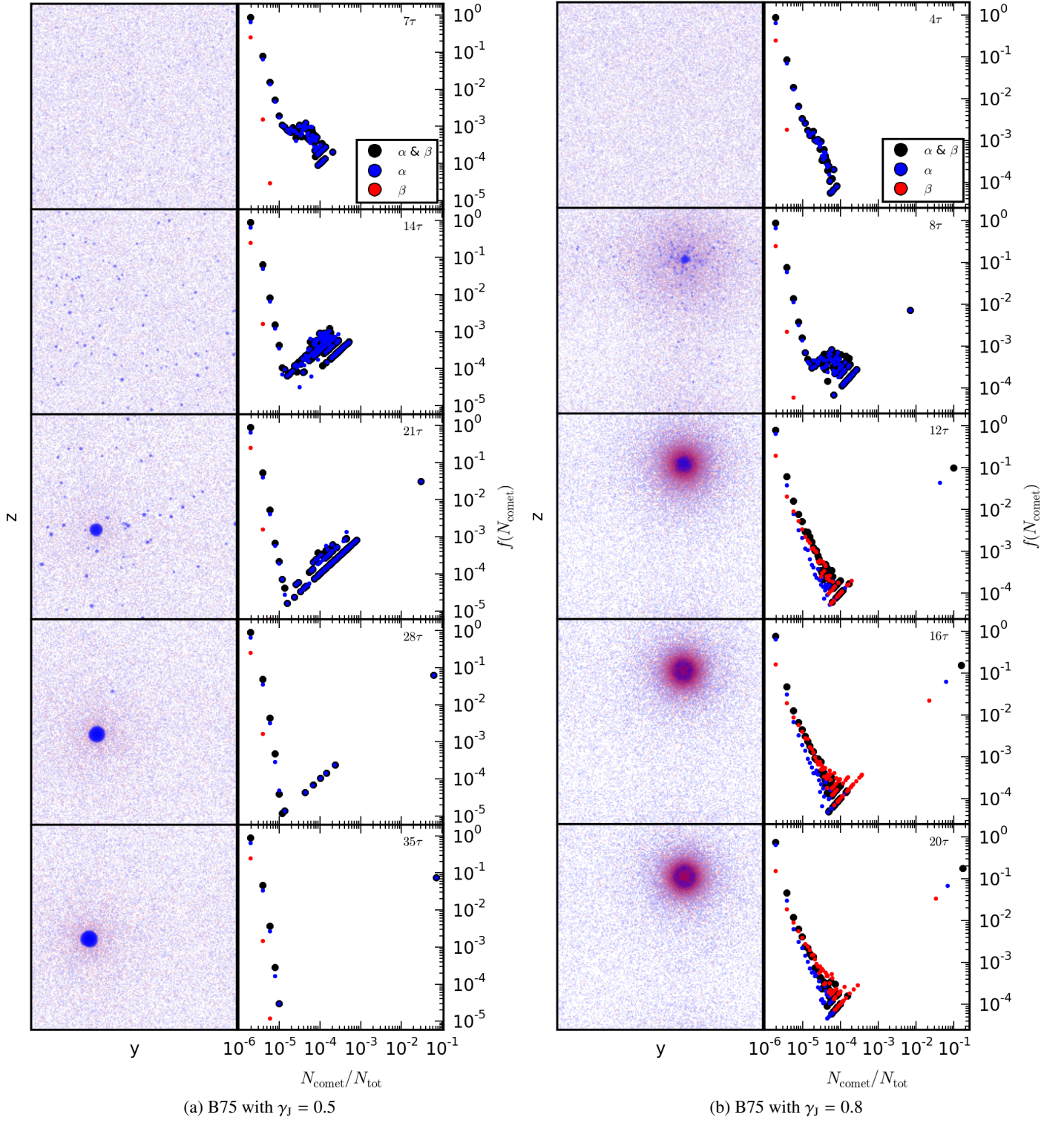


Fig. 14: Time sequence of the simulation B75. On the left side, the slice shows in depth 20% of the super-molecules. On the right side,  $N_{\text{comet}}$  is the number of super-molecules in one comet and  $f(N_B)$  is the comet size distribution function.



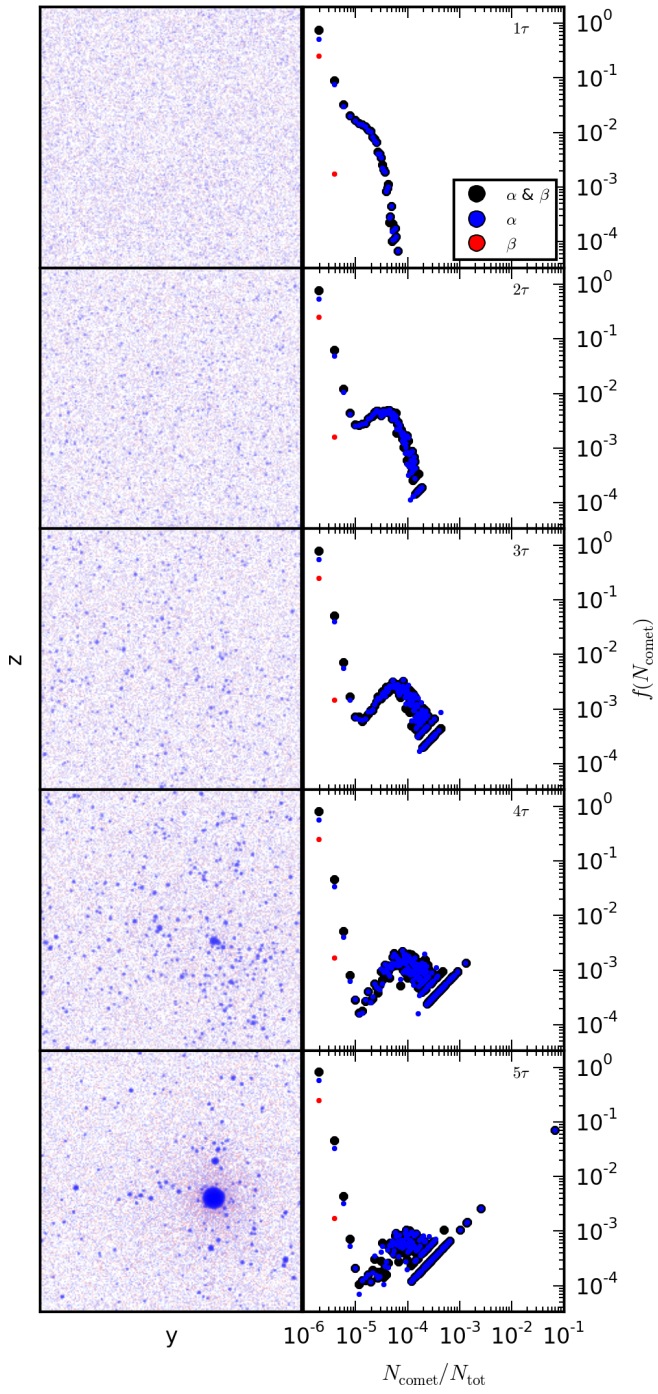


Fig. 16: Time sequence of the simulation C75 with  $\gamma_G = 1.5$ . On the left side, the slice shows in depth 20% of the super-molecules. On the right side,  $N_{\text{comet}}$  is the number of super-molecules in one comet and  $f(N_B)$  is the comet size distribution function.